Chem Soc Rev

REVIEW ARTICLE

View Article Online
View Journal





Cite this: DOI: 10.1039/c7cs00266a

# Symmetry strategies for high performance lanthanide-based single-molecule magnets

Jun-Liang Liu, Yan-Cong Chen and Ming-Liang Tong *

Received 16th October 2017

DOI: 10.1039/c7cs00266a

rsc.li/chem-soc-rev

Toward promising candidates of quantum information processing, the rapid development of lanthanide-based single-molecule magnets (Ln-SMMs) highlights design strategies in consideration of the local symmetry of lanthanide ions. In this review, crystal-field theory is employed to demonstrate the electronic structures according to the semiquantitative electrostatic model. Then, specific symmetry elements are analysed for the elimination of transverse crystal fields and quantum tunnelling of magnetization (QTM). In this way, high-performance Ln-SMMs can be designed to enable extremely slow relaxation of magnetization, namely magnetic blocking; however, their practical magnetic characterization becomes increasingly challenging. Therefore, we will attempt to interpret the experimental behaviours and clarify some issues in detail. Finally, representative Ln-SMMs with specific local symmetries are summarized in combination with the discussion on the symmetry strategies, and some of the underlying questions are put forward.

## 1. Introduction

Single-molecule magnets (SMMs) have attracted enormous and multidisciplinary research studies in the past few decades, since their non-trivial memory effect and quantum phenomena give rise to their potential applications in ultra-high density data storage, quantum computing and spintronics.[1–8] In addition, as a system between the microscopic and macroscopic worlds, their exceptional behaviours are of particular interest in fundamental scientific studies.

Unlike conventional bulk magnets, SMMs are quantized systems in which the spin of a molecule can be trapped in either of the bistable states. Consequently, the magnetization is retained unless it is assisted by quantum tunnelling of magnetization (QTM) or spin–lattice relaxation.[5] In recent years, lanthanide-based single-molecule magnets (Ln-SMMs) have become the most eye-catching and high-performance SMMs.[9–17] For instance, the astonishing finding of $[Dy(Cp^{ttt})_2]^+$ displays a hysteresis

*MOE Key Lab of Bioinorganic and Synthetic Chemistry, School of Chemistry, Sun Yat-Sen University, Guangzhou 510275, P. R. China.*
*E-mail: tongml@mail.sysu.edu.cn*

**Jun-Liang Liu**

*Dr Jun-Liang Liu obtained his PhD degree (Materials Physics and Chemistry) in 2015 from Sun Yat-Sen University, under the supervision of Prof. Ming-Liang Tong. Following a postdoctoral fellow at the Centre de Recherche Paul Pascal, CNRS, with Dr Rodolphe Clérac, he joined SYSU as an associate researcher in 2016. His research interests are focused on the design, synthesis and analysis of molecule-based magnets, especially lanthanide-based single-molecule magnets.*

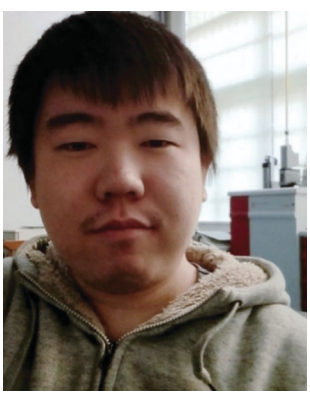

**Yan-Cong Chen**

*Dr Yan-Cong Chen obtained his PhD degree (Inorganic Chemistry) from Sun Yat-Sen University in 2017, under the supervision of Prof. Ming-Liang Tong. He has been responsible for magnetic measurements since 2012 and he is currently conducting post-doctoral research in the same laboratory supported by the National Postdoctoral Program for Innovative Talents. His research interests include the design, synthesis and characterization of various molecule-based magnetic materials such as single-molecule magnets, molecular magnetic coolants and spin crossover materials.*

opening temperature of 60 K, approaching the liquid nitrogen region,[18,19] which further demonstrates the great potential of Ln-SMMs.

However, the magnetic dynamics of most Ln-SMMs are still far from satisfactory. It is believed that the fast spin–lattice relaxation and QTM limit the ceiling of relaxation time, especially for single-ion magnets (SIMs) with only one paramagnetic ion. Therefore the suppression of QTM is very important not only to increase the effective energy barrier ($U_{eff}$) by relaxing through higher excited magnetic states, but also to increase the blocking temperature ($T_B$) below which magnetization is considered frozen.

In pursuit of high-performance SMMs with a considerable memory effect, the key goal is to seek for efficient and chemically feasible routes against the reversal of magnetization. Since the intrinsic magnetism of SMMs is closely related to chemical structure, the rapid development of this area raises higher and ongoing expectation on understanding the magneto-structural correlations. As a simple model, a SIM is apparently the good prototype for achieving such a goal. In the comprehension of single-ion anisotropy, crystal-field theory reveals the importance of a local coordination environment to the electronic structures of $Ln^{III}$ ions. According to the electrostatic model which is old but intuitive,[20–25] regulating the charge distribution symmetry should work theoretically and practically in the design and synthesis of high-performance Ln-SMMs.

In this review, we will focus on the introduction of an efficient and feasible symmetry strategy based on crystal-field theory, including fundamental theory and optimized blue prints. By the analysis of the angular distribution of the electrostatic potential, the oblate- and prolate-symmetric preferences and energy level crossings of magnetic states are explained. In addition, the ''systematic absences'' of the transverse crystal-field terms are concisely and intuitively demonstrated, aiming at hindrance to the reversal of magnetization by minimizing the transverse magnetic anisotropy and narrowing the tunnel splitting. It is proposed that the strategy of using specific symmetries, including $C_n$ ($n \geq 7$), $S_8/D_{4d}$, $C_{5h}/D_{5h}$ and $S_{12}/D_{6d}$,[26] can be helpful in the design of high-performance Ln-SMMs.

At the same time, high-performance SMMs bring greater challenges and problems in the experimental magnetic characterization. We would also like to discuss some important practical concerns in detail, including the static and dynamic magnetic characterization, based on the analysis from their corresponding theoretical models and our experiences.

Then, we would present an overview of some Ln-SMMs reported in recent years. Their magneto-structural correlations are discussed in the aspects of symmetry strategies. Finally, based on the fulfilment of symmetry strategies, we raise several open questions and have an outlook of some important challenges for the future development of high-performance SMMs.

**Ming-Liang Tong**

*Prof. Ming-Liang Tong obtained his PhD from Sun Yat-Sen University in 1999, under the supervision of Prof. Xiao-Ming Chen. Then he joined the faculty at SYSU and was promoted to a Professor in 2004. In 2001, he worked as a JSPS postdoctoral fellow with Prof. Susumu Kitagawa in Kyoto University. He was elected as ''Changjiang Scholar'' in 2014 by the Ministry of Education and he is currently vice dean of the School of Chemistry, SYSU. His research interests cover low-dimensional molecular magnets (SMMs and SCMs), cryogenic molecular magnetic coolants, spin crossover and multifunctional molecular materials.*

## 2. Theoretical background

In this section, we will focus on giving an intelligible theoretical background of the crystal-field effect using the effective charge model, and the basic rules of symmetry strategies, accompanied by the recipes for achieving the goal toward high-performance Ln-SMMs.

### 2.1 Electronic structure of tripositive lanthanide ions

For paramagnetic tripositive lanthanide ions from $Ce^{III}$ ($4f^1$) to $Yb^{III}$ ($4f^{13}$), the ground electron configurations are $[Xe]4f^n$, whose 4f electrons are efficiently shielded by the outer electrons of the 5s and 5p orbitals. As a consequence, their energy spectra are much inert to the environment; thus the coordination complexes behave like the free ions with the near degeneracy of the 4f orbitals, compared with those of d valence electrons.

On account of the Russell–Saunders coupling scheme and Hund's rule, the ground terms of the electronic structures of $Ln^{III}$ ions are well described as the term symbols of $^{2S+1}L_J$ (Table 1). Such multiplets are further split by the crystalline electric field or crystal field (CF), leading to $2J + 1$ pure or superimposed magnetic states ($m_J$) with the integer interval

Table 1 Calculated electronic and magnetic parameters for the $Ln^{III}$ free ions

| $Ln^{III}$ | $4f^n$, $n$ = | Ground term $^{2S+1}L_J$ | Landé $g_J$ factor | Curie constant [$cm^3$ K $mol^{-1}$] |
|---|---|---|---|---|
| Ce | 1 | $^2F_{5/2}$ | 6/7 | 0.80 |
| Pr | 2 | $^3H_4$ | 4/5 | 1.60 |
| Nd | 3 | $^4I_{9/2}$ | 8/11 | 1.64 |
| Pm | 4 | $^5I_4$ | 3/5 | 0.90 |
| Sm | 5 | $^6H_{5/2}$ | 2/7 | 0.09 |
| Eu | 6 | $^7F_0$ | — | 0 |
| Gd | 7 | $^8S_{7/2}$ | 2 | 7.88 |
| Tb | 8 | $^7F_6$ | 3/2 | 11.82 |
| Dy | 9 | $^6H_{15/2}$ | 4/3 | 14.17 |
| Ho | 10 | $^5I_8$ | 5/4 | 14.07 |
| Er | 11 | $^4I_{15/2}$ | 6/5 | 11.48 |
| Tm | 12 | $^3H_6$ | 7/6 | 7.15 |
| Yb | 13 | $^2F_{7/2}$ | 8/7 | 2.57 |

from $-J$ to $+J$. Specifically, for the Kramers system with odd-number fermions, the magnetic states will split into several pairs of Kramers doublets (KDs), each of which contains one eigenstate and its time-reversed state ($\hat{C}|\mathrm{KD}_1\rangle = |\mathrm{KD}_2\rangle$, and $\hat{C}$ is the time-reversal operator; $\hat{J}_z|\mathrm{KD}_1\rangle = +\hbar M|\mathrm{KD}_1\rangle$, $\hat{J}_z|\mathrm{KD}_2\rangle = -\hbar M|\mathrm{KD}_2\rangle$). In the presence of purely electric fields, the eigenvalues of KDs must be equal ($\hat{H}_{\mathrm{CF}}|\mathrm{KD}_{1(\mathrm{or}\,2)}\rangle = E|\mathrm{KD}_{1(\mathrm{or}\,2)}\rangle$). In other words, the KDs are all at least doubly degenerate in CFs without any magnetic field, according to the Kramers theorem.[23,27,28]

With respect to the $^{2S+1}\mathrm{L}_J$ term, the Landé $g_J$ factor (eqn (2.1)) is naturally introduced by the cosine rule. The free-ion Curie constants can be calculated accordingly, and the experimental values of room-temperature molar magnetic susceptibility $\chi T$ should be close to the free-ion Curie constants of $N\mu_B{}^2 g_J{}^2 J(J+1)/3k_B$ ($N$: Avogadro constant; $\mu_B$: Bohr magneton; $k_B$: Boltzmann constant).[29]

$$g_J = \frac{3}{2} + \frac{S(S+1) - L(L+1)}{2J(J+1)} \tag{2.1}$$

### 2.2 Crystal-field effect

Early in 1929, Bethe introduced the effective charge model, followed by the discussion on the energy splitting and the influence of CF symmetries.[30] A variety of other crystal-field models, such as the superposition model,[31] the simple overlap model,[32] the semiempirical radial effective charge model[33] and *ab initio* calculations,[34] have been proposed to further consider other effects besides solely electrostatic repulsion.

The crystal-field effect, which principally arises from the Coulomb interaction between the electrons of the central metal ion and the outer coordination ligands, is essential for Ln-SMMs, since it is critical to the splitting of multiplets and to the probability of magnetization reversal. In general, coordination compounds can be simplified as two parts outside a metal nucleus: a 4f-electron shell from the metal ion ("ion field") and a ligand shell from the coordination atoms ("crystal field").

Let's consider the "ion field" first. The $\mathrm{Ln}^{\mathrm{III}}$ is at the origin, and the 4f electrons are supposed to locate at $\vec{r}$. In this scheme, the electrostatic potential ($V_{\mathrm{IF}}$) of the "ion field" in the position of $\vec{R}$ ($R > r$) can be described as the summation of all 4f electrons according to Coulomb's law (eqn (2.2)).[22–25,35]

$$V_{\mathrm{IF}}(\vec{R}) = \int \frac{\rho_{\mathrm{M}}(\vec{r})}{|\vec{R} - \vec{r}|} \mathrm{d}\tau \tag{2.2}$$

where $\rho_{\mathrm{M}}$ is the volumetric charge density of the 4f shell, and $\mathrm{d}\tau = r^2 \sin\theta \mathrm{d}r\mathrm{d}\theta\mathrm{d}\varphi$ is the volume element in a spherical coordinate system. It is worth noting that all physical quantities are based on atomic units, in which elementary charge and Coulomb's constant are both unity.

Considering multipole expansion and addition theorem for spherical harmonics, eqn (2.2) can be shown as the summation of all terms of the $2^k$ ($k$ = 0, 1, 2,...) spherical multipole moments ($Q_{kq}$) and the irregular solid harmonics ($I_{kq}$),[35] which, respectively, correspond to the "ion field" and the "crystal field". The definitions of the above products are involved in spherical harmonics ($Y_k^q$).

$$V_{\mathrm{IF}}(\vec{R}) = \sum_{k=0}^{\infty} \sum_{q=-k}^{k} \left[ \frac{4\pi}{2k+1} Q_{kq} \cdot I_{kq}(\vec{R}) \right]$$

$$Q_{kq} \equiv \int r^k \cdot \left[ Y_k^q(\vec{r}) \right]^* \cdot \rho_{\mathrm{M}}(\vec{r}) \mathrm{d}\tau \tag{2.3}$$

$$I_{kq}(\vec{R}) \equiv \frac{Y_k^q(\vec{R})}{R^{k+1}}$$

The volumetric charge density of the 4f shell is the spatial distribution of radial and angular dependences. Sievers calculated the charge density of a certain $|J, \pm m_J\rangle$ state for $\mathrm{Ln}^{\mathrm{III}}$ ions,[36] whose axially-symmetric ($C_\infty$) angular distribution can be visualized as the hydrogen-like atomic orbitals in Scheme 1. He also proposed that the angular-momentum-dependent $Q_{kq}$ can be simply expressed as the product of the multipole moment coefficients ($c_{\mathrm{Ln},k}$, see ref. 36) and the expectation values of $r^k$ ($\langle r_{\mathrm{Ln}}^k \rangle = \int f(r)^2 r^k r^2 \mathrm{d}r$, where $f(r)$ is the 4f radial wavefunction):[23,36,37]

$$Q_{kq}(m_J) = \langle r_{\mathrm{Ln}}^k \rangle c_{\mathrm{Ln},k}(m_J) \tag{2.4}$$

where $c_{\mathrm{Ln},k}$ are derived multipole efficiencies and linearly proportional to the $k$-order Stevens coefficients ($\Theta_{\mathrm{Ln},k}$) and can be obtained using the Wigner–Eckart theorem.[36,38–40]

Specifically, for pure 4f ions, only the spherical multipole moments of $k$ = 0, 2, 4, 6 are necessary, because (1) the azimuthal quantum number of 4f orbitals ($l$) is 3 and (2) the odd-$k$ spherical harmonics are of odd parity, thus $Q_{kq}$ and $V_{\mathrm{IF}}$ become zero (eqn (2.3)). By ignoring the high-order anisotropy, Skomski simplified the angular distribution of charge density with the quadrupole moment ($k$ = 2) term alone, showing that $\mathrm{Ce}^{\mathrm{III}}$, $\mathrm{Pr}^{\mathrm{III}}$, $\mathrm{Nd}^{\mathrm{III}}$, $\mathrm{Tb}^{\mathrm{III}}$, $\mathrm{Dy}^{\mathrm{III}}$ and $\mathrm{Ho}^{\mathrm{III}}$ are oblate-symmetric, whereas $\mathrm{Pm}^{\mathrm{III}}$, $\mathrm{Sm}^{\mathrm{III}}$, $\mathrm{Er}^{\mathrm{III}}$, $\mathrm{Tm}^{\mathrm{III}}$ and $\mathrm{Yb}^{\mathrm{III}}$ are prolate-symmetric, which is equivalent to the result of axial zero-field splitting ($D$).[41] According to this, Rinehart and Long summarized a qualitative method for enhancing the axial magnetic anisotropy.[42] The idea

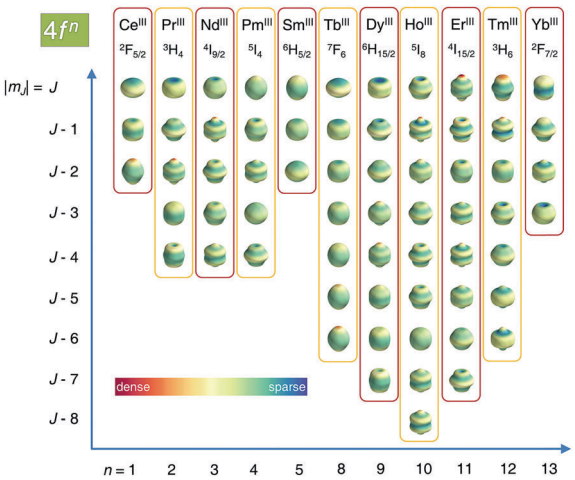


Scheme 1 Visualization of the $m_J$-dependence angular distribution of charge density for lanthanide(III) 4f shells. This scheme is calculated based on ref. 36.

is to minimize the electrostatic repulsion between the $Ln^{III}$ ground-$m_J$ charge density and the ligand charge density. This concise and intuitive model has been acting as a very beneficial guide to the design of Ln-SMMs.

In addition, the electrostatic interaction is also dependent on the distances between central $Ln^{III}$ and outer ligands. For the sake of better discussion semiquantitatively, the electrostatic potential can be calculated. Combining eqn (2.3) with eqn (2.4), the aspherical $m_J$-dependent electrostatic potential is shown in eqn (2.5) in further considering the screening factors ($\sigma_{Ln,k}$).[24,25,37] It should be mentioned that the monopole moment ($k = 0$) term is indeed an $m_J$-independent or spherical electrostatic potential, which does not affect the crystal-field energy levels; therefore, it is omitted for clarity. The "crystal field" effect is now introduced:

$$V_{IF}(R,\theta,m_J) = \sum_{k=2,4,6}\left[\frac{4\pi}{2k+1}(1-\sigma_{Ln,k})\langle r_{Ln}^{k}\rangle c_{Ln,k}(m_J)\frac{Y_k^0(\theta)}{R^{k+1}}\right] \quad (2.5)$$

Suppose that the coordination atoms are discrete point charges with the effective charge of $Z_{eff,j}$ on the $j$th coordination site, according to the point-charge electrostatic (PCE) model, the electrostatic energy ($E_{PCE}$) should be the summation of all ligand sites:

$$E_{PCE}(m_J) = \sum_{j}^{ligand} Z_{eff,j} V_{IF}(R_j,\theta_j,m_J) \quad (2.6)$$

Just the same as the Rinehart–Long model, the qualitative or semiquantitative application of eqn (2.5) and (2.6) is valid only if (1) the transverse magnetic anisotropy of the "crystal field" from the outer ligands is totally absent, namely all eigenstates are pure, for instance in axial symmetry; (2) the $z$-axis of the frame of reference must be along the quantized axis, because the calculated charge densities and multipole moments herein are based on the specific $|J, \pm m_J\rangle$ state of the ground term $^{2S+1}L_J$. For low-symmetry $Ln^{III}$ complexes, the ignorance of transverse magnetic anisotropy and the mismatch of the principal axes could bring more or less deviation, depending on the symmetry of charge distribution.

With the above concerns, the search for magnetic anisotropy axes is very important. Besides *ab initio* calculations and experimental determinations, another possible route is to minimize the electrostatic energy.[15,43–47] Chilton *et al.* developed an electrostatic model and software called MAGELLAN for readily predicting the magnetic anisotropy axes for $|m_J| = 15/2$ states for $Dy^{III}$ ions.[21] Jiang *et al.* improved the model and applied it to some complexes with $Tb^{III}$, $Dy^{III}$, and $Er^{III}$.[48]

Provided that the above conditions are met, the electrostatic potential can be calculated based on eqn (2.5) as depicted in Scheme 2, assuming the potential surfaces with a Ln–X distance of 2.3 Å (typical for Ln–O/N). From the potential surfaces, semiquantitative energy levels can be directly obtained by summation of all charges. For example, when a $Ce^{III}$ is located between two axially coordinated charges with an effective charge of $Z_{eff} = 1e$ for each, the energy levels are estimated as $e[V_{IF}(2.3\text{ Å}, 0, m_J) + V_{IF}(2.3\text{ Å}, \pi, m_J)]$, giving 0, 1466 and 2929 K for $|m_J| = 5/2$, 3/2 and 1/2, respectively.

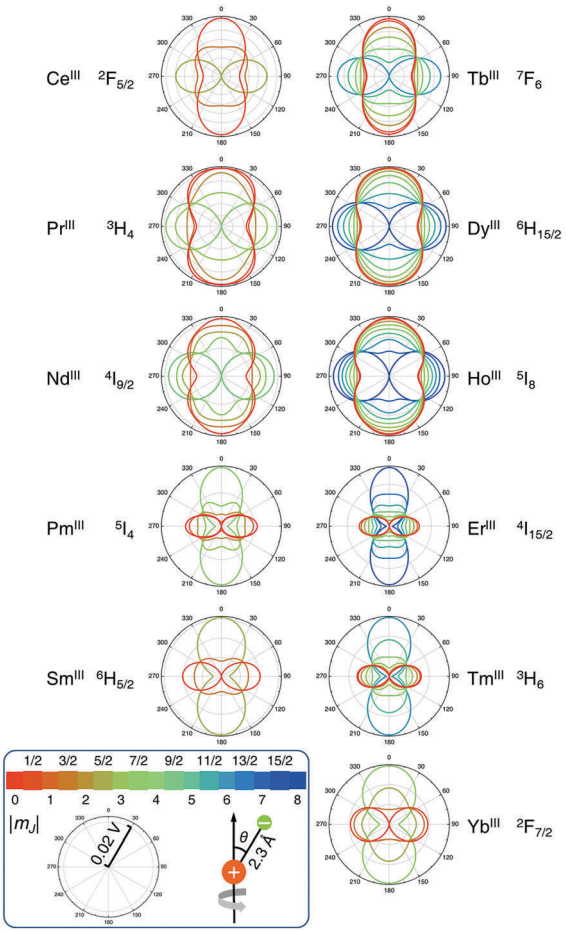


Scheme 2 Illustration of the $m_J$-dependence zenithal($\theta$)-distribution electrostatic potential for 4f shells, located at a distance of 2.3 Å away from the central lanthanide(III) ion. This scheme is calculated based on eqn (2.5), shown in the polar coordinate where the radius and polar angle represent $V_{IF}$ (0.02 V per grey circle tick) and $\theta$, respectively.

Roughly speaking, the orders of $|J, \pm m_J\rangle$ states for all $Ln^{III}$ ions are in good agreement with the intuitive model of an oblate- or prolate-symmetric $Ln^{III}$ core when the ligand charge density is axially or equatorially distributed. Taking $Dy^{III}$ as an example in Scheme 2, by allocating the point charges in axial positions, the electrostatic energy of the largest $|m_J| = 15/2$ marked as blue is the lowest and thus it is stabilized, whereas the equatorial point charges stabilize the smallest $|m_J| = 1/2$ marked as red.

However, the situation changes when the zenith angle of the charged atom is close to the so-called "magic angle" ($\theta = 54.7^\circ$) as in dipolar interactions,[49–51] nuclear magnetic resonance[52] and magnetic resonance imaging,[53] which is the special angle when the spherical harmonics $Y_2^0(\theta) = 0$. In other words, the quadrupole moment ($k = 2$) is absent in the "magic angle"; thus the electrostatic potential is dominated by the high-order terms of the hexadecapole moment ($k = 4$) and hexacontatetraple

moment ($k = 6$). The typical case is the family of $[Ln(Pc)_2]^-$ with pseudo-$D_{4d}$ symmetry, whose ground $|m_J|$ is not always the largest or smallest one, but sometimes intermediate $|m_J|$.[51] A close inspection of Scheme 2 can clearly tell that the energy level switches around the "magic angle". In this situation, the energy level is no longer ranked by the sequential $|m_J|$, which becomes more complicated and is beyond the double-well potential.

In the case of a potentially large energy barrier, the energy splitting of the ground $^{2S+1}L_J$ term can be achieved using this simple model to a great extent. However, the overwhelmingly reported Ln-SMMs relax through the lowest-lying excited states rather than the highest one. This fact demonstrates that the transverse magnetic anisotropy cannot be neglected and in fact plays a very important role in SMMs.

### 2.3 A highlight of the symmetry strategy

If the transverse magnetic anisotropy originating from the CFs is not fully quenched, which is common for Ln complexes, the operator equivalent Hamiltonian projected on the ground term $^{2S+1}L_J$ can be written as:[20,22–25,31,54–58]

$$\hat{H}_{CF} = \sum_{k=2,4,6}\sum_{q=-k}^{k} B_k^q \hat{O}_k^q(J) \tag{2.7}$$

where $\hat{O}_k^q$ are the extended Stevens operators,[59,60] which are widely used in many computation programs like EasySpin,[61] PHI[62] and SIMPRE.[56–58] The CF parameters of $B_k^q$ are all real numbers and can be explicitly expressed in eqn (2.8) as derived from the PCE model. This equation is also useful to semiquantitatively estimate the crystal-field parameters and the constraints under some specific symmetries.[22,25,30,56] The generalized effective charge models have been applied in some Ln-SIMs for calculating the energy levels and the compositions of the eigenstates.[20,58,63,64]

$$B_k^q = \begin{cases} \dfrac{4\pi(1-\sigma_{Ln,k})\langle r_{Ln}^k\rangle \Theta_{Ln,k} w_{k0}}{2k+1} \sum_j^{ligand} \left\{ \dfrac{Z_{eff,j}}{R_j^{k+1}} Y_k^0(\theta_j,\varphi_j) \right\} & (q=0) \\ \dfrac{8\pi(1-\sigma_{Ln,k})\langle r_{Ln}^k\rangle \Theta_{Ln,k}(-1)^q w_{kq}}{2k+1} \sum_j^{ligand} \left\{ \dfrac{Z_{eff,j}}{R_j^{k+1}} \mathrm{Re}\left[ Y_k^q(\theta_j,\varphi_j) \right] \right\} & (q>0) \\ \dfrac{8\pi(1-\sigma_{Ln,k})\langle r_{Ln}^k\rangle \Theta_{Ln,k}(-1)^q w_{k|q|}}{2k+1} \sum_j^{ligand} \left\{ \dfrac{Z_{eff,j}}{R_j^{k+1}} \mathrm{Im}\left[ Y_k^{|q|}(\theta_j,\varphi_j) \right] \right\} & (q<0) \end{cases} \tag{2.8}$$

In eqn (2.8), $w_{kq}$ are the prefactors of the spherical harmonics $Y_k^q$,[20,25,56] and all other parameters are identical to those mentioned in Section 2.2. When all the terms of $q \neq 0$ are absent, namely without transverse magnetic anisotropy, the results of eqn (2.7) and eqn (2.8) are equivalent to that of eqn (2.6).

The presence of transverse CFs $B_k^q (q \neq 0)$, though usually weak for performant Ln-SMMs, would couple the magnetic states with $\Delta m_J/q$ = integer and change the energy levels slightly as perturbation. In this situation for non-Kramers ions, the energy difference (or tunnel splitting, $\Delta_{tun}$) between the perturbed ($|\alpha\rangle$ and $|\beta\rangle$) and the unperturbed states ($|M\rangle$ and $|M'\rangle$) is intrinsic. According to the perturbation theory, the magnitude of tunnel splitting is shown in eqn (2.9). For Kramers ions, the Kramers theorem ensures at least doubly degeneracy under strictly zero magnetic field. However, the internal transverse magnetic field from the surroundings ($H_\varepsilon$, like magnetic dipolar interactions, hyperfine interactions, *etc.*) is unavoidable and could also yield $\Delta_{tun}$ *via* a transverse magnetic field, as shown in eqn (2.10).[65,66] It is also worth noting that $\Delta_{tun}$ for the ground Kramers doublet can be synergistically magnified by the transversal Zeeman effect and the transverse CFs.

$$\Delta_{tun} \approx 2|\langle M'|\hat{H}_{CF,q\neq 0}|M\rangle| \tag{2.9}$$

$$\Delta_{tun} \approx 2g_J\mu_B \sqrt{\sum_{i\in(x,y)} \left[ |\langle KD_2|\hat{J}_i|KD_1\rangle|^2 {H_{\varepsilon,i}}^2 \right]} \tag{2.10}$$

The non-zero off-diagonal matrix elements coming from the transverse CFs and/or Zeeman effect prevent the doublet from crossing ("avoided crossing") along with tunnel splitting. Two extreme scenarios are shown in Scheme 3: when the external-field sweeping rate is extremely slow, namely the quantum adiabatic process, the SMM remains in its original $n$th eigenstate (for example $|\alpha\rangle$) from beginning to end, according to the adiabatic theorem in quantum mechanics.[28] As a result, the expectation value of the magnetic moment ($\mu_i = -dE_i/dH$) changes from $\mu_M$ to $\mu_{M'}$, which is well known as QTM. On the other hand, when the external-field sweeping rate is extremely fast, the SMM remains in its initial state (for example $|M\rangle$); thus, the magnetic moment remains unchanged.

The tunnelling transition probability ($P_{tun,\mu\rightarrow\mu'}$) in a two-level system can be derived from the Landau–Zener formula in eqn (2.11).[66–70] This demonstrates that the tunnelling probability

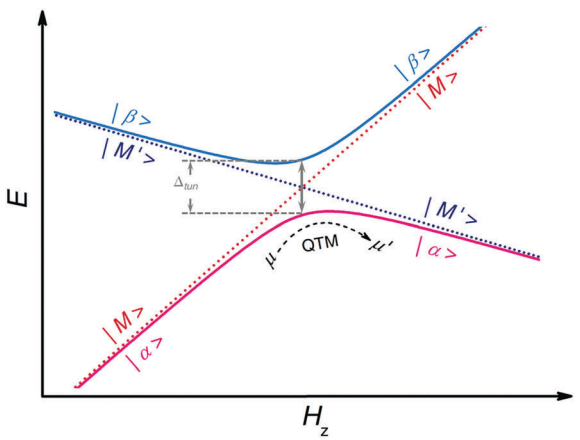


Scheme 3 Quantum tunnelling of magnetization under the quantum adiabatic process (solid lines) and the quantum diabatic process (dashed lines) with the tunnel splitting of $\Delta_{tun}$.

can be facilitated by large tunnel splitting, a small external-field sweeping rate ($dH/dt$) and a small change in magnetic moments.

$$P_{\mathrm{tun},\mu\to\mu'} = 1 - \exp\left(-\frac{\pi {\Delta_{\mathrm{tun}}}^2}{2\hbar\frac{dH}{dt}|\mu_{\mathrm{M}} - \mu_{\mathrm{M}'}|}\right) \quad (2.11)$$

QTM gives rise to the reversal of magnetization and therefore limits the performance of SMMs. Since the magnitude of $\Delta_{\mathrm{tun}}$ depends on the corresponding $\Delta m_J$ values, their energy differences and the magnitudes of transverse CFs, some promising strategies are straightforward to suppress QTM: (1) to stabilize the ground doublet with large $|m_J|$; (2) to enlarge the energy differences between the ground and the excited states; and (3) to vanish the transverse CFs as far as possible. The former two strategies can be applied as illustrated in Section 2.2.

For the 3rd strategy, crystal-field theory has provided clues to eliminate degrees of freedom under specific symmetries.[20,22,24,25,30,71] To suppress QTM, the strategy is to minimize the sum of transverse crystal-field terms ($q \neq 0$) in the braces found in eqn (2.8), which is defined as $F_{kq}$ in eqn (2.12). If $F_{kq} = 0$, the transverse crystal-field parameters $B_k^q(q \neq 0)$ would be absent. It is apparent that all $F_{kq}$ are dependent on the symmetry of the coordinates ($R$, $\theta$, $\varphi$) and the effective charge distributions ($Z_{\mathrm{eff}}$). In further consideration of rotation symmetry, $F_{kq}$ is proportional to $F_{kq}'$ in eqn (2.13), where $P_k^q$ is the associated Legendre polynomials.

$$F_{kq} = \sum_j^{\text{ligand}} \left\{\frac{Z_{\mathrm{eff},j}}{R_j^{k+1}} Y_k^q\left(\theta_j, \varphi_j\right)\right\} \quad (q \neq 0) \quad (2.12)$$

$$\begin{aligned} F_{kq}' &= \sum_j^{\text{ligand}} Y_k^q\left(\theta_j, \varphi_j\right) \\ &= w_{kq} \sum_j^{\text{ligand}} P_k^q\left[\cos\left(\theta_j\right)\right] \exp\left(iq\varphi_j\right) \ (q \neq 0) \end{aligned} \quad (2.13)$$

Next, we are going to intuitively demonstrate how the local symmetries of charge distribution eliminate transverse CFs. To some extent, it is similar to the systematic absences or selection rules to specific symmetries in the area of crystallography or spectroscopy.

**2.3.1 Rotation, $C_n$.** The spherical coordinates of a series of point charges in $C_n$ rotation symmetry can be written as $(\theta_0, \varphi_0 + 2\pi j/n)$, $0 \leq j \leq n-1$.

$$F_{kq}' = Y_k^q(\theta_0, \varphi_0) \cdot \sum_{j=0}^{n-1} \exp\left(i\frac{q}{n}2\pi j\right) = 0 \quad \left(\frac{|q|}{n} \neq \text{integer}\right) \quad (2.14)$$

By summing up a geometric series, it is clear that all transverse CF parameters vanish when $|q|/n \neq$ integer. For example, an SMM with the charge distribution of 5-fold rotation symmetry would eliminate all CF parameters except for $B_k^{\pm 5}$. When higher rotation symmetry ($n \geq 7$) is applied, all $B_k^q(q \neq 0)$ become zero since $k = 2$, 4, and 6 and $|q|$ cannot be larger than $k$. In particular, for $Ce^{III}$ and $Sm^{III}$ with $J = 5/2$, all $B_k^q$ ($q \neq 0$) will be zero when $n \geq 5$.

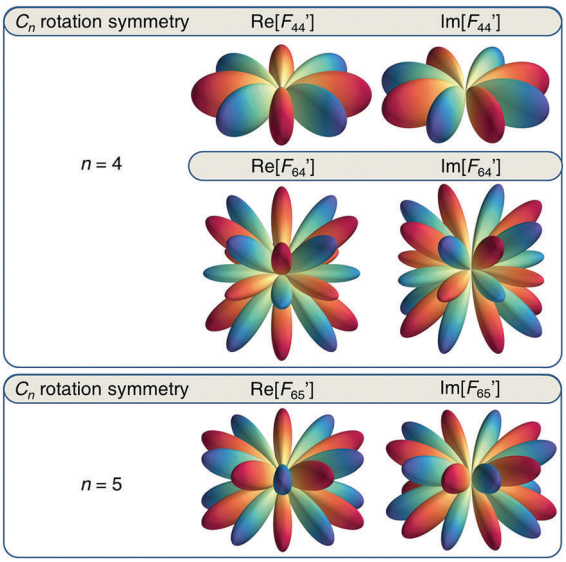


Scheme 4 Illustration of the angular distribution of the selected non-zero $F_{kq}'$ in the real (Re) and imaginary (Im) parts, under the corresponding $C_n$ ($n$ = 4 or 5) rotation symmetry. The red region denotes the positive values, while the blue one denotes the negative values.

**2.3.2 Mirror in the equatorial plane, $\sigma_h$.** Similar to the rotation operator, one point charge at $(\theta_0, \varphi_0)$ would generate another one located at $(\pi - \theta_0, \varphi_0)$. Employing the parity of the spherical harmonics, eqn (2.15) indicates that all $B_k^q(q \neq 0)$ will be zero when $q$ = odd integer, because $k$ must be even integer.

$$F_{kq}' = Y_k^q(\theta_0, \varphi_0) \cdot \left[1 + (-1)^{k+q}\right] = 0 \quad (q = \text{odd}) \quad (2.15)$$

Scheme 4 illustrates the non-vanishing $F_{kq}'$ in the real and imaginary parts under specific rotation symmetries. If the charge distribution exhibits $C_5$ symmetry (hence $F_{65}' \neq 0$) together with a mirror $\sigma_h$, denoting a $C_{5h}$ symmetry, the red and blue regions will cancel each other out due to the parity. That is to say, all transverse CFs vanish under the $C_{5h}$ symmetry.

**2.3.3 Improper rotation, $S_n$ ($n \geq 2$ and even).** Combining a rotation axis with a mirror plane, $F_{kq}'$ will be zero on condition that either $|q|/n$ = half-integer with $q$ = even integer or $|2q|/n \neq$ integer. When $n = 8$ ($S_8$), for example a square antiprism. As shown in Scheme 4, the regions above and below the mirror plane will cancel each other out in the contribution to $F_{44}'$ and $F_{64}'$, so all $B_k^q(q \neq 0)$ will be zero.

$$\begin{aligned} F_{kq}' &= Y_k^q(\theta_0, \varphi_0) \\ &\times \left[1 + (-1)^{k+q} \exp\left(i\frac{q}{n}2\pi\right)\right] \sum_{j=0}^{n/2-1} \exp\left(i\frac{2q}{n}2\pi j\right) \end{aligned} \quad (2.16)$$

On applying the aforementioned rules, the systematic absences or selection rules are listed in Table 2. When the charge

 

Table 2 Systematic absences of transverse crystal-field terms ($k$ = 2, 4, 6)

| Point group | $C_n$, $n$ = | $\sigma_h$ | $S_n$, $n$ = | Selection rule $F_{kq}' = 0$ when $\|q\|$ = | Suppression of QTM |
|---|---|---|---|---|---|
| $C_s$ | 1 | ✔ | — | 1, 3, 5 | — |
| $C_i/S_2$ | 1 | — | 2 | — | — |
| $C_1$ | 1 | — | — | — | — |
| $C_2$ | 2 | — | — | 1, 3, 5 | — |
| $C_3$ | 3 | — | — | 1, 2, 4, 5 | — |
| $C_4$ | 2, 4 | — | — | 1, 2, 3, 5, 6 | — |
| $C_5$ | 5 | — | — | 1, 2, 3, 4, 6 | — |
| $C_6$ | 2, 3, 6 | — | — | 1, 2, 3, 4, 5 | — |
| $C_n$ ($n \geq 7$) | $\geq 7$ | — | — | All | ✔ |
| $C_{2h}$ | 2 | ✔ | — | 1, 3, 5 | — |
| $C_{3h}$ | 3 | ✔ | 3 | 1, 2, 3, 4, 5 | — |
| $C_{4h}$ | 2, 4 | ✔ | 4 | 1, 2, 3, 5, 6 | — |
| $C_{5h}$ | 5 | ✔ | 5 | All | ✔ |
| $C_{6h}$ | 2, 3, 6 | ✔ | 3, 6 | 1, 2, 3, 4, 5 | — |
| $S_4/D_{2d}$ | 2 | — | 4 | 1, 2, 3, 5, 6 | — |
| $S_6/D_{3d}$ | 3 | — | 6 | 1, 2, 4, 5 | — |
| $S_8/D_{4d}$ | 2, 4 | — | 8 | All | ✔ |
| $S_{10}/D_{5d}$ | 5 | — | 10 | 1, 2, 3, 4, 6 | — |
| $S_{12}/D_{6d}$ | 2, 3, 6 | — | 4, 12 | All | ✔ |

distribution is under any local symmetry of $C_n$ ($n \geq 7$ including $C_\infty$, namely high-order axial symmetry), $C_{5h}/D_{5h}$ (pentagonal bipyramid/pentagonal prism), $S_8/D_{4d}$ (square antiprism/bicapped square antiprism) and $S_{12}/D_{6d}$ (hexagonal antiprism), all transverse CF parameters vanish and thus would be greatly beneficial for suppression of QTM. Actually all of these four classes of molecular point groups have been explicitly proposed to design SIMs for such purposes.[26]

Let's talk about the chosen of principal axis. Any sets of coordinates along with arbitrary rotations or reflections can result in identical eigenvalues of eqn (2.7), albeit distinct eigenvectors. However, in consideration of the direction that contributes most for the highly anisotropic $Ln^{III}$ ion in SMMs, we should notice that the principal axis of the coordinate system should be chosen as the easy axis of the ground doublet, along which the magnetic moment is maximum. This reveals that the symmetry rule for the suppression of QTM is valid when the molecular principal axis coincides with the magnetic easy axis, reminding the importance of stabilizing the large $|m_J|$ states.

Recognizing the symmetry rule for the suppression of QTM, we successfully achieved the first pseudo-$C_{5h}/D_{5h}$ Ln-SIM in 2013.[26] The weak and 5-fold arrangement of the equatorial coordination atoms for $\{DyZn_2\}_{D_{5h}}$ diminishes the transverse CFs and exhibits much better performance than the desolvated $\{DyZn_2\}_{O_h}$ (pseudo-$O_h$ local symmetry) which bears larger energy splitting though.

On closer inspection of spherical harmonics with $q \neq 0$ as in Scheme 4, one can find that all $F_{kq}'$ become very small if the ligands are located closely to the axial position. For the oblate-symmetric $Ln^{III}$, it is better to allocate the axial ligands more linear in aspects of suppressing QTM and enhancing energy barriers. On the other hand, it is possible that Ln-SMMs still show a good performance in the absence perfect linearity, which is a result of *ab initio* calculations for $Dy^{III}$.[72] In fact, $B_k^q(q \neq 0)$ values could remain small if not zero in theory. However, the magnitudes of $B_k^q(q \neq 0)$ are highly dependent on the $Ln^{III}$ species (eqn (2.8)). For instance, $[Dy(Cp^{ttt})_2]^+$ demonstrates very good SMM performance, while other heavy lanthanide metalloceniums are far behind because the ground states are highly mixed, or with the smallest $|m_J|$.[73]

Unfortunately, none of these symmetries exist in all 32 crystallographic point groups, suggesting that it is impossible to realize such perfect symmetries in conventional crystalline compounds. Nevertheless, we can still attempt to make it as close as possible. We should strengthen again that the transverse CF parameters $B_k^q(q \neq 0)$ (or $F_{kq}$) can be very small or even accidentally vanished, although the symmetry is far from perfect. In such situations, the residual $F_{kq}$ from one ligand could be compensated for by other asymmetric ligands. Moreover, the effective charges of the ligands are not necessary localized at the centres of the coordinated atoms. The analysis of charge displacements and magnitudes is complicated, depending on the character of the ligands, especially for the ligands with delocalized charges.

Besides static CFs, the interaction between spin and lattice vibration called spin–phonon coupling is one of the key factors for spin–lattice relaxation, which is also vital to the performance of SMMs.[18,74–76] Magnetic relaxation processes like Orbach, Raman, direct and other mechanisms are strongly dependent on magnetic energy states, phonon spectra and spin–phonon coupling.[23,74–81] For clarity, spin–phonon coupling herein is simplified as the dynamic CFs, accounting for the ligand displacements relative to the metal centre. Hence the dynamic CFs can be written as the Taylor expansion of the crystal field potential ($V_{CF}$) with respect to the displacements.[23,77–81] The 1st order derivatives of the spherical harmonics are shown as eqn (2.17),[77]

$$\frac{\partial V_{CF}}{\partial x} \sim \frac{\partial Y_k^0}{\partial x} \sim \frac{Y_{k-1}^1 - Y_{k-1}^{-1}}{2}$$
$$\frac{\partial V_{CF}}{\partial y} \sim \frac{\partial Y_k^0}{\partial y} \sim \frac{Y_{k-1}^1 + Y_{k-1}^{-1}}{2i} \quad (2.17)$$
$$\frac{\partial V_{CF}}{\partial z} \sim \frac{\partial Y_k^0}{\partial z} \sim Y_{k-1}^0$$

suggesting that the vibration of the coordination ligands can produce the transverse CFs ($B_k^q$, $q \neq 0$) by destroying the molecular symmetry, thus accelerating the spin–lattice relaxation according to Fermi's golden rule.[23,28,79] This implies that we should consider the symmetry of both static and dynamic crystal structures, constraining and minimizing the molecular vibrations that possibly violate the transition selection rule. Nevertheless, the symmetry of the static structure is still very important because the spin–phonon transitions are closely related to the transverse magnetic anisotropy.[82–84]

## 3. Practical concerns about magnetic studies

The symmetry strategy, when effectively applied, opens a promising gate for the design and synthesis of high-performance

Ln-SMMs with large energy barriers and long relaxation times. As a side effect, multiple challenges and problems will emerge in their practical magnetic characterization and data analysis. Here, we will try to clarify some practical concerns starting from the static magnetism of a highly anisotropic spin, and then move on to the dynamic behaviour of a model system, explaining and unifying the common characterization based on a simple relaxation equation. Detailed issues that need to be taken into account are discussed at the same time.

### 3.1 Static magnetization and magnetic susceptibility

The static magnetization ($M$) and magnetic susceptibility ($\chi = \mathrm{d}M/\mathrm{d}H$) clearly reveal the magnetic moment and magnetic anisotropy of lanthanide SMMs. Compared with the free-ion magnetic susceptibility (Table 1), the experimental $\chi T$ value at room temperature is usually close to but lower, which is owing to the splitting of energy levels up to hundreds of $\mathrm{cm}^{-1}$ in the aspherical CF. Upon decreasing the temperature, a steady decrease of $\chi T$ values is usually observed owing to the depopulation of higher energy levels rather than solely antiferromagnetic interactions. Therefore, a routine Curie–Weiss fitting of magnetic susceptibility does not represent the magnitude of antiferromagnetic interactions; instead one must consider a comprehensive fitting employing the crystal-field parameters for highly anisotropic Ln-SMMs.

Then, let's calculate the average magnetization of a powder sample for a highly anisotropic $Ln^{III}$ ion with an Ising-like ground doublet that is well separated with the excited ones. In spherical coordinates, any direction ($\theta$, $\varphi$) for the pseudo-spin-1/2 with $g_{\mathrm{eff},x} = g_{\mathrm{eff},y} = 0$, $g_{\mathrm{eff},z} \neq 0$ gives the energy spectrum under an applied field ($H$) of $E_i(\theta,\varphi) = \pm 1/2 g_{\mathrm{eff},z}\mu_{\mathrm{B}} H\cos(\theta)$, where $\mu_{\mathrm{B}}$ is the Bohr magneton. Therefore, the partition function $Z$ can be written as:

$$\begin{aligned} Z &= \exp[\cos(\theta)\cdot x] + \exp[-\cos(\theta)\cdot x] \\ x &= \frac{1}{2} g_{\mathrm{eff},z}\frac{\mu_{\mathrm{B}} H}{k_{\mathrm{B}} T} \end{aligned} \tag{3.1}$$

where $k_{\mathrm{B}}$ is the Boltzmann constant. And the magnetic moment along this direction is:

$$m(\theta,\varphi) = N k_{\mathrm{B}}\frac{\partial \ln Z}{\partial H} = \frac{1}{2} g_{\mathrm{eff},z}\cos(\theta)\tanh(\cos(\theta)x) N\mu_{\mathrm{B}} \tag{3.2}$$

from which the average magnetization of the powder sample can be calculated by the integral as $M = 1/(4\pi)\int\int m(\theta,\varphi)\sin\theta \mathrm{d}\theta\mathrm{d}\varphi$. Finally,

$$\begin{aligned} M &= \frac{1}{4} g_{\mathrm{eff},z} f(x) N\mu_{\mathrm{B}} \\ f(x) &= 1 - \frac{1}{x^2}\left[\mathrm{Li}_2\left(1+\mathrm{e}^{-2x}\right) + \frac{\pi^2}{12}\right] + \frac{2}{x}\ln\left(1+\mathrm{e}^{-2x}\right) \end{aligned} \tag{3.3}$$

where $\mathrm{Li}_2$ is Spence's function, or dilogarithm:

$$\mathrm{Li}_2(x) = \int_0^x \frac{\ln(t)}{1-t}\mathrm{d}t \tag{3.4}$$

First of all, we can notice that $M$ is a function of $g_{\mathrm{eff},z}$ and $H/T$. Therefore, a series of $M$ *vs.* $H/T$ curves for a Ln-SMM with Ising-like anisotropy should perfectly overlap with each other, which is also confirmed by the experimental results. This situation is different from those of moderate-performance SMMs (whose $M$ *vs.* $H/T$ curves are separated), but somehow similar to the Brillouin function for isotropic spins, despite that the shapes of the curves are different (Scheme 5).

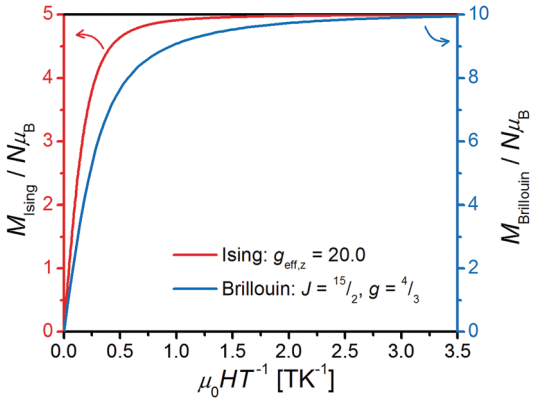


Scheme 5 *M vs. H/T* curves for an Ising-like ion compared with the Brillouin function.

Then, when it goes to the low-field limit where $\chi = M/H$, the magnetic susceptibility product $\chi T$ can be solved as:

$$\chi T = \lim_{H/T\to 0}\frac{M}{H}T = \frac{N\mu_{\mathrm{B}}{}^2}{3k_{\mathrm{B}}}\frac{1}{4} g_{\mathrm{eff},z}{}^2 \approx \frac{g_{\mathrm{eff},z}{}^2}{32} \tag{3.5}$$

and it corresponds well with the common $\chi T \approx 12.5\ \mathrm{cm}^3\ \mathrm{K\ mol}^{-1}$ at low temperature for most of the $Dy^{III}$ SMMs with $|m_J| = 15/2$ ground doublets, especially for SIMs where magnetic exchange is absent.

Alternatively, when it goes to the high-field limit, the saturation magnetization is:

$$M_{\mathrm{sat}} = \lim_{H/T\to\infty} M = \frac{1}{4} g_{\mathrm{eff},z} N\mu_{\mathrm{B}} \tag{3.6}$$

which is considerably lower than the straightforward value of $g_J N\mu_{\mathrm{B}}$ and easily account for most of the performant $Dy^{III}$ SIMs ($|m_J| = 15/2$, $g_{\mathrm{eff},z} \approx 20$) showing $M_{\mathrm{sat}}$ only $\approx 5N\mu_{\mathrm{B}}$ rather than $10N\mu_{\mathrm{B}}$.

Owing to such large anisotropy for most of the $Ln^{III}$ ions, a significant torque can be generated in the magnetic field. If the sample is not sufficiently immobilized (by Vaseline or eicosane), the rotation of the crystals is highly possible. As a result, the magnetization will deviate from that of random-oriented powders. Such a situation can be easily identified by the irreproducible experimental values, especially when a large field has been applied in between (for example, checking $\chi T$ for a second time after measuring $M$–$H$ curves).

### 3.2 Slow magnetic relaxation and blocking temperature

The most important and characteristic behaviour of SMMs must be their slow relaxation of magnetization, which is a dynamic process and is thus time-dependent. Under thermal equilibrium conditions, the equilibrium magnetization $M_{\mathrm{eq}}$ for a specific

 

system equals the static magnetization discussed in Section 3.1. When the rearrangement of the magnetic moment is slower than the alteration of the temperature or magnetic field, the instant magnetization will differ from $M_{eq}$. To regain thermal equilibrium, the system can go through spin–lattice relaxation as described by a differential equation (Bloch equation):[5,23]

$$\frac{dM(t,T,H)}{dt} = -\frac{M(t,T,H) - M_{eq}(t,T,H)}{\tau(T,H)} \quad (3.7)$$

where $\tau$ is the relaxation time and its reciprocal $\tau^{-1}$ is the overall relaxation rate calculated by summing up various kinds of processes:[5,23,76,79,85,86]

$$\tau(T,H)^{-1} = \tau_{Orbach}(T)^{-1} + \tau_{Raman}(T)^{-1} + \tau_{direct}(T,H)^{-1} + \tau_{QTM}(H)^{-1} + \cdots \quad (3.8)$$

It should be noted that, as long as a magnetic system follows eqn (3.8) at any specific field and temperature, it will have a single relaxation time despite the combination of different processes. In contrast, the observation of multiple relaxation times is possible for complicated systems with different magnetic species such as many multinuclear Ln-SMMs with crystallographically inequivalent Ln sites.[87] By decently setting up the conditions for phenomenological eqn (3.8), the time-dependent magnetization arising from the slow relaxation of magnetization can be revealed. To facilitate the following discussion on a series of magnetic behaviours and their dependence on various factors, here we first establish a hypothetical system with typical parameters for Ln-SMMs as:

$$\tau(T,H)^{-1} = 10^{10}e^{-\frac{400}{T}} + 10^{-6}T^5 + 10^{-2}H^4T + \frac{10}{1+10^8H^2} \quad (3.9)$$

which is a nice SMM with $U_{eff}$ = 400 K, followed by a Raman process with $n$ = 5, and the QTM/direct process dominating the low temperature region (Scheme 6). It should be noted that eqn (3.9) also accounts for the field-dependence (inset of Scheme 6) as the applying of an external field could suppress QTM by reducing the superimposition of pseudo-degenerate states. At the same time, the direct process would be promoted.

It should be noted that the overall relaxation times of these processes are largely dominated by the smallest one at each position (*e.g.* Orbach process at high temperature and QTM at low temperature for $H_{dc}$ = 0 Oe). This situation is easy to understand as the system would largely relax through the fastest route, whereas the slow routes do not contribute much.

With the relaxation time differing by several orders of magnitude, a different technique must be applied to fully characterize the relaxation process. At higher temperature, a conventional AC magnetometer can easily cover the $10^{-5}$–$10^{0}$ s range. This is achieved by applying an oscillating AC magnetic field ($H_{ac}$) and a DC field ($H_{dc}$) (if necessary) to the sample:

$$H = H_{ac}\sin(\omega t) + H_{dc} \quad (3.10)$$

where the angular frequency $\omega = 2\pi\nu$ and $\nu$ is the AC linear frequency. Then the amplitude and phase ($\varphi$) of magnetization are measured and usually converted into complex magnetic

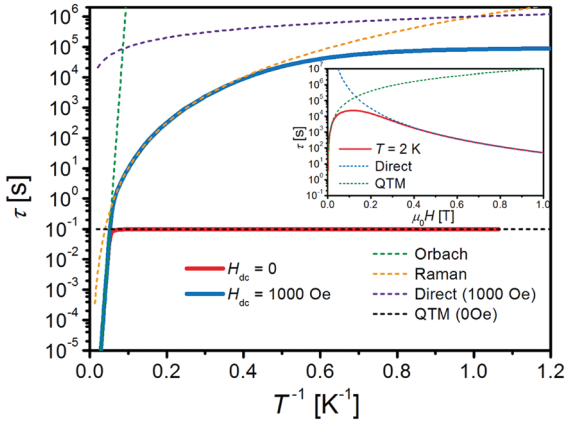


Scheme 6 Temperature and field dependence (inset) of relaxation time for a hypothetical system. Dashed lines represent the contributions from different relaxation processes.

susceptibilities, namely the in-phase $\chi'$ and out-of-phase $\chi''$ (inset of Scheme 7). Here, the equilibrium magnetization becomes:

$$M_{eq}(t,T,H) = M_{eq,ac}(t,T,H_{ac}) + M_{eq,dc}(T,H_{dc}) = \chi_{ac}(T,H_{dc})H_{ac}\sin(\omega t) + \chi_{dc}(T,H_{dc})H_{dc} \quad (3.11)$$

where $\chi_{ac}$ and $\chi_{dc}$ are AC/DC isothermal magnetic susceptibilities, respectively. Therefore, eqn (3.7) becomes:

$$\frac{dM(t,T,H)}{dt} = -\frac{[M(t,T,H) - \chi_{dc}(T,H_{dc})H_{dc}] - \chi_{ac}(T,H_{dc})H_{ac}\sin(\omega t)}{\tau(T,H_{dc})} \quad (3.12)$$

A typical numerical solution of eqn (3.12) is shown in Scheme 7 in frequency-dependent AC susceptibility. When the oscillating frequency is far slower than the relaxation of magnetization, there is little phase shift and the in-phase susceptibility $\chi'$ matches well with the static $\chi$. With increasing frequency, the magnetization lags behind the AC magnetic field. The out-of-phase

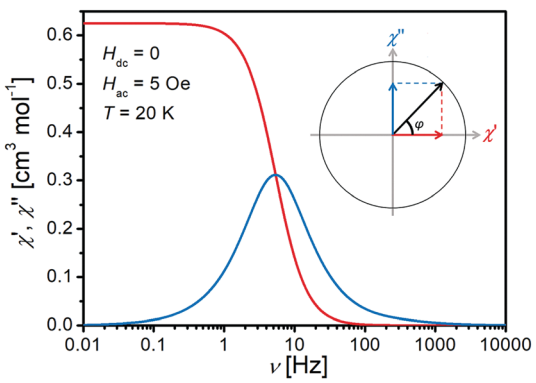


Scheme 7 Frequency dependence of AC susceptibility for a hypothetical system. Inset: The decomposition of complex susceptibility into amplitude (black) and phase ($\varphi$), or into in-phase $\chi'$ (red) and out-of-phase $\chi''$ (blue).

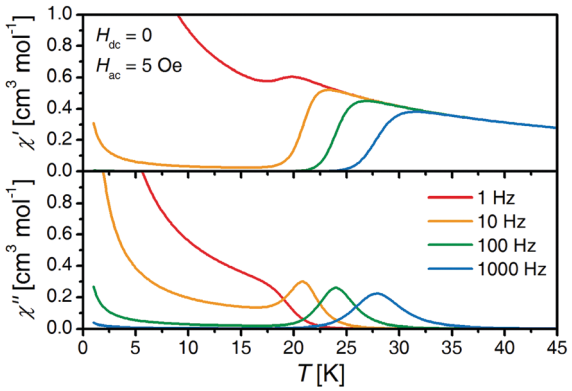


Scheme 8 Temperature dependence of AC susceptibility under zero field for a hypothetical system, with the "tails" of AC magnetic susceptibilities that are explained in the text.

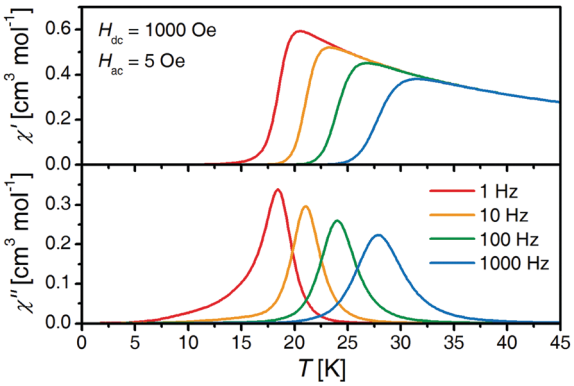


Scheme 9 Temperature dependence of AC susceptibility under a 1000 Oe static field for a hypothetical system.

susceptibility $\chi''$ starts to increase accompanied by a fall of $\chi'$. When the frequency is even higher, the magnetization begins to "block" and shows less and less response to the oscillating field, with decrease of $\chi''$. Here, the peak of $\chi''$ corresponds to the resonance, where the frequency matches the relaxation time as $\tau = 1/\omega$.

When depicted in the temperature-dependence of AC susceptibility, the situation is more complicated (Scheme 8). As shown in Scheme 6, the relaxation time increases rapidly in the high temperature range going through the Orbach process, but limited by the QTM in the low temperature range at 0.1 s (eqn (3.9) and Scheme 6) in zero field. It is easy to understand that, when the relaxation time ceases to increase, the phase shift of magnetization remains unchanged upon decreasing the temperature. However, the amplitude of the magnetization still increases in the way of $\chi'T \approx$ const., which makes the "tails" of AC susceptibilities and submerge the peaks at low frequencies (Scheme 8).

Measuring AC susceptibility in the presence of a DC field could add a more detailed picture of the relaxation dynamics. When a DC field (*e.g.* 1000 Oe) is applied here, according to eqn (3.9) the QTM is suppressed and the relaxation time is now dominated by the Raman process, which keeps increasing (Scheme 6). Still, the shape of the peak is slightly asymmetric (Scheme 9) owing to the different temperature dependencies between different relaxation processes (Orbach *vs.* Raman at 1 Hz here). As a result, the peak position of the temperature-dependent AC susceptibility is shifted and deviates from the temperature corresponding to the resonance frequency. That is the reason why one should fit the relaxation time from the frequency-dependency of AC susceptibility instead.

When the relaxation time is too long for an AC magnetometer at lower temperature, alternatively it can be calculated by directly measuring the decay curves of magnetization. This is achieved by first magnetizing the sample by a high field and then quickly removing the field (or sweep to a static field of $H_f$, if necessary), and the magnetizations through time are measured and fitted by the generalized exponential decay as:[5,66]

$$M(t) = M_f + (M_0 - M_f)\exp[-(t/\tau)^{\beta}] \qquad (3.13)$$

where $M_0$ is the initial magnetization, $M_f$ is the final magnetization, and $\beta$ is a generalized coefficient which should be 1 for an ideal exponential decay, which can be also derived from eqn (3.7) when the temperature and field are constant. However, $\beta$ is usually lower than 1 owing to the faster relaxation rate at the beginning, which may come from the impact of dipolar interactions, hyperfine interactions, magnetocrystalline anisotropy, *etc.*

Then by combining the AC and DC data, one can fit the temperature dependence of relaxation time over a wide range of temperatures and distinguish each relaxation process. Here, a commonly witnessed artefact is that one may tend to only fit several "linear" points on the obviously bending $\ln(\tau)$ *vs.* $1/T$ curve using an Arrhenius equation, assuming a dominant Orbach process. However, if the magnetic relaxation is in fact dominated by the Raman process, which is sometimes witnessed in Ln-SMMs but especially common for Yb-SMMs,[26,73,88–93] such simple Arrhenius fitting results do not represent the reality. A meaningless apparent energy barrier will be yielded, which is abnormally smaller than the real energy difference between magnetic states and is often accompanied by a large pre-exponential factor ($\tau_0$). Indeed, the linear temperature dependence of relaxation times in a log-reciprocal scale can be helpful for checking up on an Orbach process; however, the Raman/direct process shows a linear dependency in a log–log scale. Therefore, one should try plotting the relaxation times in both different scales to identify the dominant process. At the other extreme, simply starting from a complete formula of all four terms without justification can result in severe over-parameterization, which also yields meaningless values with huge estimated standard deviations.

Here we would also start questioning the term "blocking temperature" ($T_B$) usually used in the community. As just described, the slow relaxation of magnetization for molecular magnets is continuously and highly temperature-dependent. Based on the relaxation time, there is a "100 s" definition saying $T_B$ to be the temperature where the relaxation time is 100 s,[5,19,94,95] and there is also a "peak" criterion saying $T_B$ to be the temperature of a specific AC peak (1500 Hz, for example).[96,97] Although the corresponding relaxation times differ much (100 s *vs.* ~0.1 ms), it's just an artificial definition, and they shall have equal status. The key problem here is that the "blocking

 

temperature'' in these molecular magnets is only a variable parameter relying on the different judgements of ''blocking''. This is much different from those of magnetic ordering materials whose ordering temperature is a definite critical point corresponding to the discontinuity of the 1st/2nd-order differential chemical potential across the phase transition.

### 3.3 Magnetic hysteresis and ZFC/FC magnetization

**3.3.1 Magnetic hysteresis.** When the temperature is kept constant and the field is sweeping at the rate of d$H$/d$t$, eqn (3.7) can be transformed into:

$$\frac{\mathrm{d}M(t,T,H)}{\mathrm{d}H} = -\frac{M(t,T,H) - M_{\mathrm{eq}}(t,T,H)}{(\mathrm{d}H/\mathrm{d}t)\tau(T,H)} \qquad (3.14)$$

and the magnetic hysteresis loop can be simulated by solving eqn (3.14) numerically in combination with the relaxation times described by eqn (3.9) (Scheme 10).

It is easy to understand that the openings of the magnetic hysteresis loops grow bigger upon decreasing the temperature, owing to the longer relaxation times. The step around zero field, however, needs to be rationalized by the field dependence of the relaxation time (inset of Scheme 6). Owing to the presence of QTM, the relaxation time decreases by several orders of magnitude around zero field and leads to much faster approaching of $M$ to $M_{\mathrm{eq}}$, creating a step. For many Ln-SMMs with severe QTM around zero field, the magnetic hysteresis loop will even exhibit a ''butterfly'' shape without opening at zero field. When the temperature is higher, the relaxation becomes faster and the hysteresis loop is smaller.

Mathematically, the magnetic hysteresis loops will always be open when the relaxation rate is finite, but it will fall into the error range and considered ''closed'' in practical measurements. If one takes the remnant magnetization ($M_{\mathrm{R}}$) of 1% relative to the saturation magnetization ($M_{\mathrm{S}}$) as a cut-off criterion, here in this specific hypothetical system the corresponding temperature is 14.2 K, where the relaxation time is $\sim$0.1 s (Scheme 11).

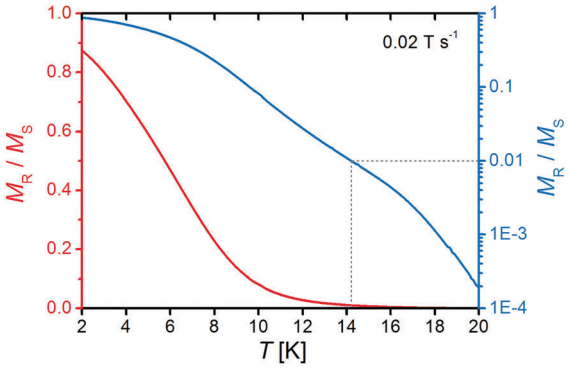


Scheme 11 Temperature dependence of remnant magnetization for a hypothetical system, depicted in normal (red) and log (blue) scales.

Practically, the measured remnant magnetization is dependent on the field-sweeping rate (Scheme 12). At low temperature where the relaxation time is relatively long, the obtained $M_{\mathrm{R}}/M_{\mathrm{S}}$ won't change much unless the field-sweeping rate is extremely slow, and it won't change much at high temperature unless the field-sweeping rate is extremely fast.

However, it should be noted that here we refer to the uniform and actual sweeping rate of the magnetic field. It is only valid for VSM or micro-SQUID that can continuously measure while sweeping the field. The conventional SQUID-based magnetometer, however, can only measure the magnetization when the field is kept steady. Therefore, the reported ''average'' sweeping rate is only a mathematical one, as each step of measurement (even in closed-loop hysteresis/driven mode) includes (1) an initialisation procedure of the magnet, (2) an actually very rapid charging of the magnet (for MPMS, it can be up to 0.02 T s$^{-1}$ and also dependent on the target field), (3) an iteration procedure to stabilize the magnet and (4) a steady platform to perform the measurement. As each of these steps takes at least several seconds, the actual sweeping rate is much faster than the reported one. Last but not least, we must stress the non-equidistant measurements (usually more points at low fields) of magnetic hysteresis loops, which are frequently witnessed in the literature, will also result in

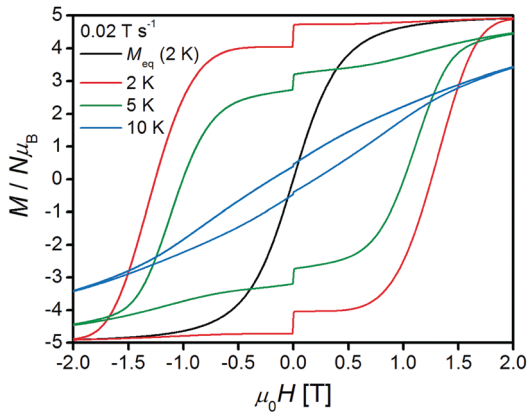


Scheme 10 Magnetic hysteresis loops for a hypothetical system, compared with the equilibrium magnetization (black) at the indicated temperatures.

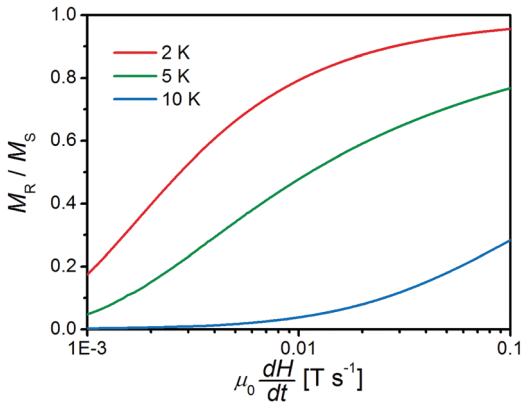


Scheme 12 Sweeping-rate dependence of remnant magnetization for a hypothetical system at the indicated temperatures.

distorted hysteresis loops or even illusive steps at which the intervals are changed.

**3.3.2 ZFC–FC magnetization.** On the other hand, when the field is kept constant and the temperature sweeps at the rate of $dT/dt$, eqn (3.7) can be transformed into:

$$\frac{dM(t,T,H)}{dT} = -\frac{M(t,T,H) - M_{eq}(t,T,H)}{(dT/dt)\tau(T,H)} \quad (3.15)$$

and the ZFC–FC magnetization can be simulated by solving eqn (3.15) numerically in combination with the relaxation times described by eqn (3.9) (Scheme 13).

For the ZFC magnetization, it is measured by cooling the sample in zero DC field, and then applying a measuring field (0.1 T herein) and recording the magnetization in warming mode during which the system is gradually magnetized. Most importantly, $M_{eq}$ is not a constant but monotonically increases upon cooling for the intrinsic paramagnets, as shown in eqn (3.5). A careful analysis of eqn (3.15) indicates that $M_{ZFC}$ and $M_{FC}$ will meet $M_{eq}$ at a peak temperature ($T_{p,ZFC}$) where $dM/dT = 0$, after which it begins to demagnetize together with the equilibrium magnetization.

The FC magnetization, however, is more interesting as the $M_{FC,cool}$–$T$ and $M_{FC,warm}$–$T$ curves represent different aspects of the magnetic relaxation between cooling/warming modes. Firstly, when the sample is cooled in a DC field (0.1 T herein), the system is gradually magnetized along the $M_{FC,cool}$–$T$ curve, which is always lower than the equilibrium magnetization and $M_{FC,cool}$ will intersect with $M_{ZFC}$ below $T_{p,ZFC}$. The lower-than-equilibrium $M_{FC,cool}$ also accounts for the drop of the $\chi T$–$T$ curve at the lowest temperature when measured in cooling mode. Then, when the magnetization is recorded in warming mode, the system is further magnetized toward $M_{eq}$. $M_{FC,warm}$ increases with a peak when it meets $M_{eq}$, after which it turns to demagnetization with a lag, leading to larger $M_{FC,warm}$ than $M_{eq}$ above $T_{p,FC,warm}$. This also suggests that if $\chi T$–$T$ measurements are performed in warming mode one may falsely attribute the peak to the hints of ferromagnetic interactions. Following the above discussions, the intersection of the $M_{ZFC}$–$T$ curve and the $M_{FC,cool}$–$T$ curve and the greater-than-equilibrium $M_{ZFC}/M_{FC,warm}$ values are both straight-forward results of the slow relaxation of magnetization as described by eqn (3.15) and shown in Scheme 13, and there is nothing to be surprised at.

Like the case of magnetic hysteresis loops, mathematically $M_{ZFC}$, $M_{FC,warm}$ and $M_{eq}$ will never meet when the relaxation rate is finite, but they will fall into the error range in practical measurements. If one takes the normalized difference of ZFC–FC magnetization of 1% as a cut-off criterion, here in this specific hypothetical system the corresponding temperature is 10 K, where the relaxation time is 10 s (Scheme 14).

What another factor must be considered here is the imperfection of ZFC magnetization in practical measurements. Firstly, the real "zero field" can never be achieved owing to the remanence field, which can be as large as 20 Oe (sometimes even opposite in sign) for conventional superconducting magnets. Charging the magnet in oscillating mode toward zero can reduce the remanence field to $<5$ Oe, but the ultra-low-field (ULF) option is necessary to satisfy higher demands. Additionally, after the system is cooled, it takes time (at least several seconds) to apply a measuring field, and the system will be partially magnetized as the relaxation time in a low field is usually quite short. Finally, if the distribution of relaxation times is wide, part of the sample could be magnetized faster than the others. As a result, the $M_{ZFC}$ curve usually begins with a non-zero value and the obtained peak temperature will become lower (dashed line in Scheme 13).

Practically, the measured peak temperature of ZFC susceptibility is largely dependent on two factors: the measuring field and the temperature-sweeping rate (Scheme 15). Recalling the field dependence of the relaxation time (inset of Scheme 6), the QTM effect is pronounced when the measuring field is low and the system will relax very rapidly. Usually a relatively larger optimized field (0.1 T herein) is used in ZFC–FC measurements. For the temperature-sweeping rate, it is monotonically related to the peak temperature. However, the fine thermal conductance between the sample and holder must be considered when rapidly sweeping the temperature, which can cause fake discrepancy between ZFC and FC magnetization even for a normal paramagnet.

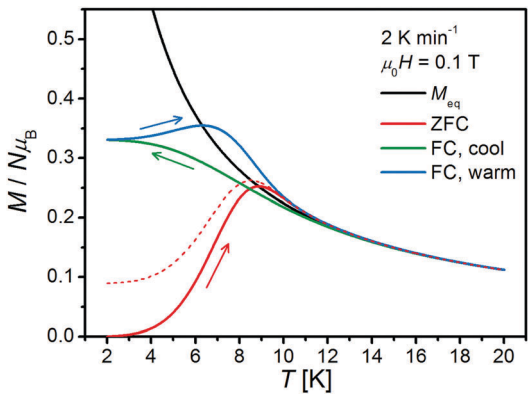


Scheme 13 ZFC–FC magnetization for a hypothetical system, compared with the equilibrium magnetization. The dashed line simulates the imperfect zero-field condition in practical measurements.

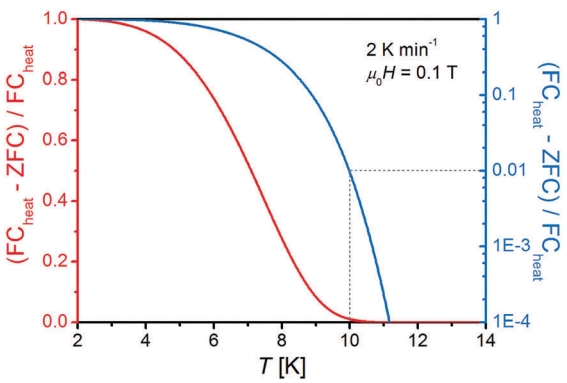


Scheme 14 Temperature dependence of the normalized difference of ZFC–FC magnetization for a hypothetical system, depicted in normal (red) and log (blue) scales.

 

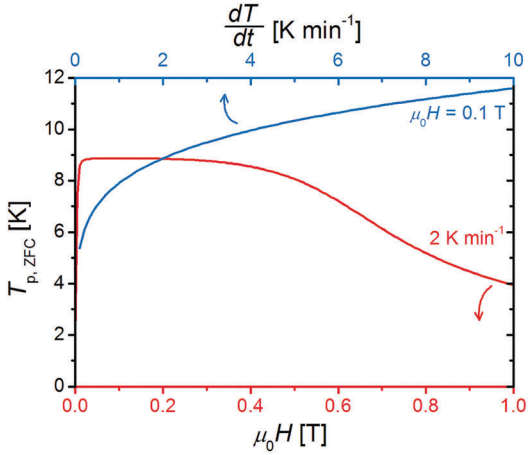


Scheme 15 Field dependence (red) and sweeping-rate dependence (blue) of the peak temperature of ZFC magnetization for a hypothetical system.

At this point, one can realize that the magnetic relaxation behaviours characterized by hysteresis and ZFC–FC magnetization also do not correspond to a single "blocking temperature", but depend on the specific experimental conditions. That's the reason why we would prefer reporting the detailed parameters (Table 3) to compare among different SMMs to avoid confusion.

### 3.4 Magnetic studies on diluted and isotopically enriched samples

Intermetallic magnetic interactions in Ln-SMMs can largely affect the magnetic relaxation behaviour, mainly through the magnetic dipolar interaction as represented by the simplified form of the dipolar field ($B_{dip}$) arising from the neighbouring magnetic moment ($\mu_i$) and the potential energy ($E_{dip}$):[49]

$$\vec{B}_{dip} = \frac{1}{d^3}[3(\vec{\mu}_i\vec{v})\vec{v} - \vec{\mu}_i]$$
$$E_{dip} = -\vec{\mu}_j\vec{B}_{dip} \quad (3.16)$$

where $v$ is the unit vector along the line between the two magnetic moments ($\mu_i$, $\mu_j$). The sign of the interaction depends on the angles between the orientation of the magnetic moments and the line connecting them, and the magnitude is further dependent on the magnetic moments and the distance ($d$) between them.

For monometallic SMMs, or SIMs, the magnetic dipolar interaction is usually weak, but still unneglectable. Although there is no chemical bonding between them, billions of molecules densely packing nearby in the bulk samples can produce noticeable magnetic dipolar interactions in the intermolecular way. Therefore, diluted samples of SIMs are sometimes necessary to investigate in spite of the long intermetallic distance

Table 3 Selected lanthanide-based single-molecule magnets with specific local symmetry of the $Ln^{III}$ ion

| Name[a] | Pseudo local symmetry | $U_{eff}$ [K] ($\mu_0H$ [T]) | Hysteresis $T_{hy}$ [K] ($\mu_0$d$H$/d$t$ [mT s$^{-1}$]) | ZFC peak $T_{p,ZFC}$ [K] (d$T$/d$t$ [K min$^{-1}$], $H$ [T]) | Selected experimental $\tau$ [s] ($T$ [K], $\mu_0H$ [T]) | Ref. |
|---|---|---|---|---|---|---|
| $[TbPc_2]^-$ | $S_8/D_{4d}$ | 331[b] (0) | 1.7 (2.7)[g] | — | 0.016 (4.5, 0) | 98 |
| [Tb(Pc)(Pc′)] | $S_8/D_{4d}$ | 939[b] (0) | 2[d,i] | — | $1.6 \times 10^{-4}$ (52, 0) | 114 |
| $[Er(W_5O_{18})_2]^{9-}$ | $S_8/D_{4d}$ | 55.2[b] (0) | — | — | $1.6 \times 10^{-4}$ (5, 0) | 115 |
| $[DyP_5W_{30}O_{110}]^{12-}$ | $C_5$ | 24[b] (0) | 2 (33[e]) | — | $5 \times 10^{-6}$ (2, 0) | 117 |
| $[DyZn_2(TTTT^{Br})_2(MeOH)]^+$ | $C_{5h}/D_{5h}$ | 439[b] (0) | 11 (20[e]) | — | 0.36 (2, 0)<br>6000 (2, 0.1) | 26 |
| [Dy(bbpen)Br] | $C_{5h}/D_{5h}$ | 1025[b] (0) | 14 (20[e]) | 9.5 (2, 0.2) | 41 (4, 0)<br>1825 (4, 0.2) | 99 |
| $[Dy(OPCy_3)_2(H_2O)_5]^{3+}$ | $C_{5h}/D_{5h}$ | 543[b] (0)<br>543[b] (0.1) | 20 (20[e]) | 11 (2, 0.1) | 21.3 (2, 0)<br>1409 (5, 0.1) | 100 |
| $[Dy(O^tBu)_2(py)_5]^+$ | $C_{5h}/D_{5h}$ | 1815[c] (0) | 4 (1.2[f])<br>8.8[i] (1.2[f]) | 14 (—[h], 0.2) | 1 (38, 0) | 124 |
| $[Er\{N(SiMe_3)_2\}_3]$ | $C_{3v}$ | 122[b] (0) | 1.9[d,i] | — | 0.7 (4, 0) | 127 |
| $[CeCd_3(Hquinha)_3(^nBu_3PO)_2I_6]$ | $C_{6h}/D_{6h}$ | Raman (0.15) | — | — | 0.038 (2.2, 0.15) | 88 |
| [(Cp*)Er(COT)] | $C_\infty$ | 197[b], 323[b] (0) | 1.8 (0.92[f])[g]<br>5[i] (0.92[f]) | 4 (—[h], 0.1)[g] | 874 (2.5, 0) | 136 |
| $[Er(COT)_2]^-$ | $C_\infty$ | 212[b] (0) | 10 (0.78[f]) | 9 (—, 0.1)[g] | 0.11 (15, 0)[g] | 141 |
| $[Er_2(COT'')_3]$ | $C_\infty$ | 323[b] (0) | 7 (2.2[f])<br>12[i] (2.2[f]) | — | 0.7 (15, 0) | 146 |
| $[Dy(Cp^{ttt})_2]^+$ | $C_\infty$ | 1837[b]/1760[b] (0) | 60 (3.9/2.2[f]) | 45/40 (2, 0.1/0.9, 0.1) | 100 (53, 0) | 18 and 19 |
| $Dy_2ScN@C_{80}$ | $C_n$ ($n \geq 7$) | 1735[b] (0) | 7 (2.9[f]) | 7 (2, —) | — | 150 |
| $Dy_2@C_{80}(CH_2Ph)$ | $C_n$ ($n \geq 7$) | 613[c] (0) | 21 (2.9[f]) | 21.9 (5, 0.2) | 100 (18, 0) | 151 |
| $[Dy(acac)_3(H_2O)_2]$ | $\sigma_h$ | 66.1[b] (0) | 0.5[i] (0.25[f])[g] | 2.4 (—, 0.08)[g] | — | 152 |
| $[Dy_5O(O^iPr)_{13}]$ | $C_{4v}$ | 528[b] (0) | — | — | 0.32 (3, 0) | 156 |
| $[Dy_4K_2O(O^tBu)_{12}]$ | $C_{4v}$ | 692[b], 316[b] (0) | 5 (140[e]) | — | — | 158 |
| $[Dy(BIPM^{TMS})_2]$ | $S_4/D_{2d}$ | 721[c], 813[c] (0) | 10 (3.5[f])[g] | 10 (0.189, 0.1) | 0.5, 1.9 (22, 0) | 159 |

Abbreviations: $H_2Pc$ = phthalocyanine; $H_2Pc'$ = ($p$-$^t$Bu-($C_6H_4$)O)$_8$Pc; $H_3TTTT^{Br}$ = 2,2′,2″-(((nitrilotris(ethane-2,1-diyl))tris(azanediyl))tris-(methylene))tris-(4-bromophenol); $H_2$bbpen = $N$,$N'$-bis(2-hydroxybenzyl)-$N$,$N'$-bis(2-picolyl)ethylenediamine; $OPCy_3$ = tricyclohexylphosphine oxide; $H_2$quinha = quinaldichydroxamic acid; Cp* = pentamethylcyclopentadienide; COT = cyclooctatetraenide; COT″ = 1,4-bis(trimethylsilyl)-cyclooctatetraenide; $Cp^{ttt}$ = 1,2,4-tri(*tert*-butyl)cyclopentadienide; acac = acetylacetonate; $H_2BIPM^{TMS}$ = $H_2C(PPh_2NSiMe_3)_2$. [a] Lattice solvent/uncoordinated molecules and counterions are not listed. [b] Energy barrier obtained from an Arrhenius law. [c] Energy barrier obtained from the best fit with a sum of different relaxation processes. [d] Field-sweeping rate unknown. [e] Continuous field-sweeping rate. [f] Average field-sweeping rate. [g] Diluted sample. [h] Temperature-sweeping rate unknown. [i] Butterfly-shaped hysteresis without observable remanence at zero field.

up to the order of 10 Å.[98–100] Thanks to the similar coordination behaviour among lanthanide ions, diluting a small amount of magnetic lanthanide ions in the isostructural diamagnetic matrix (*e.g.* $Y^{III}$) is a commonly used way. For multinuclear clusters, intramolecular magnetic interactions are obvious and play an important role in magnetism. Performing magnetic studies on diluted multinuclear clusters could reveal the single-ion behaviour and clarify the impact of magnetic interactions. Sometimes it is also an interesting strategy to take advantage of the lanthanide contraction and perform the dilution into specific coordination sites, where the large $La^{III}$ and small $Lu^{III}$ can be used instead of the intermediate $Y^{III}$.[101]

Another unneglectable factor that could be considered is the hyperfine interaction, namely the interplay between nuclear spins and electron spins, which generate a series of hyperfine magnetic states along with multiple level crossings that can suppress or facilitate QTM. For those lanthanide ions with only one natural isotope (*e.g.* $^{159}$Tb and $^{165}$Ho), such interaction is evidenced by the multiple transitions in electron paramagnetic resonance (EPR), the steps in magnetic hysteresis loops and the non-monotonic/periodic field dependence of the relaxation times.[102–106] However, the mostly studied $Dy^{III}$ ion is mainly a mixing of four abundant stable isotopes ($^{161–164}$Dy), in which $^{161/163}$Dy has a nuclear spin of $I$ = 5/2 and $^{162/164}$Dy has no nuclear spin. Performing magnetic studies on isotopically enriched samples (usually accompanied by diamagnetic dilution) are useful to investigate their potentially distinct magnetic dynamics, respectively.[107,108]

## 4. Recent advances of symmetry strategies in lanthanide-based single-molecule magnets

In this section, we will give a detailed and comprehensive survey of several classes of Ln-SMMs with specific local symmetries, combining the discussion of symmetry strategies. The detailed parameters for magnetic relaxation are listed in Table 3 along with the abbreviations for ligands.

### 4.1 $S_8/D_{4d}$

As discussed in the symmetry strategy, the crystal field of perfect $S_8/D_{4d}$ symmetry would cancel out its contribution to non-zero $F_{kq}'$ terms (Scheme 4). It should be mentioned that, for the continuous shape measure (CShM) values calculated using the SHAPE program,[109] the zenithal angle ($\theta$) of a perfect square antiprism is defined as the "magic angle" (54.7°). However, this is actually not necessary for $S_8/D_{4d}$ symmetry, so a large CShM value is not equivalent to a significant deviation from perfect $S_8/D_{4d}$ symmetry.

In Ln-SMMs, the eight-coordinated square antiprismatic geometry falls into this category and promotes the most well-studied family of {Ln(Pc)$_2$}. It all began with the double-decker (TBA)[Tb(Pc)$_2$] (TBA = $N(C_4H_9)_4^+$),[98] where the $Tb^{III}$ is confined between two $Pc^{2-}$ ligands in a staggered conformation (Fig. 1). The peak of $\chi''$ is observed at 11.5 K for 997 Hz, and the diluted

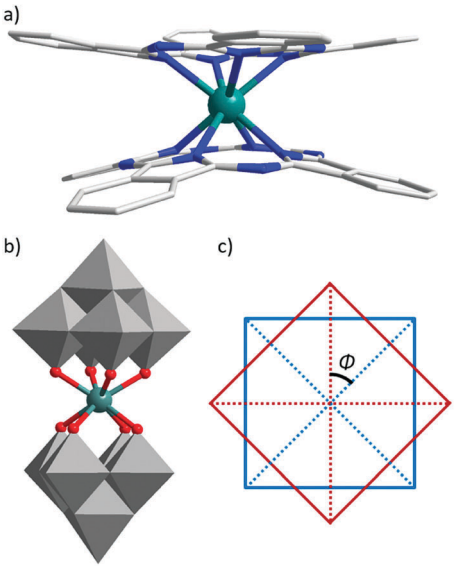


Fig. 1 Molecular structures of $[Pc_2Ln]^-$ (a) and $[Er(W_5O_{18})_2]^{9-}$ (b), and the definition (c) of the twist angle ($\Phi$).

sample (1 : 4) exhibits an energy barrier of 331 K at zero field. A detailed study on the energy levels shows the ground doublet of $[Tb(Pc)_2]^-$ is $|m_J|$ = 6, while that of the isostructural $[Dy(Pc)_2]^-$ is $|m_J|$ = 13/2 (rather than the largest 15/2).[51] It could be rationalized as the CFs provided by the $Pc^{2-}$ ligands are not located at the axial position but in the oblique direction. In addition to the crystal-field potential in Scheme 2, here we further present the ground $m_J$ states for different zenithal angles ($\theta$) and Ln–X distances (Scheme 16). It is clear that the ground doublet of $Tb^{III}$ would be $|m_J|$ = 6 as long as $\theta < 55°$. However, taking the Ln–X distance of 2.3 Å as an example, the $|m_J|$ = 15/2 states of $Dy^{III}$ would cease to be the lowest for $\theta > 49°$, which is much smaller than that of $Tb^{III}$. The equivalent negative charges from

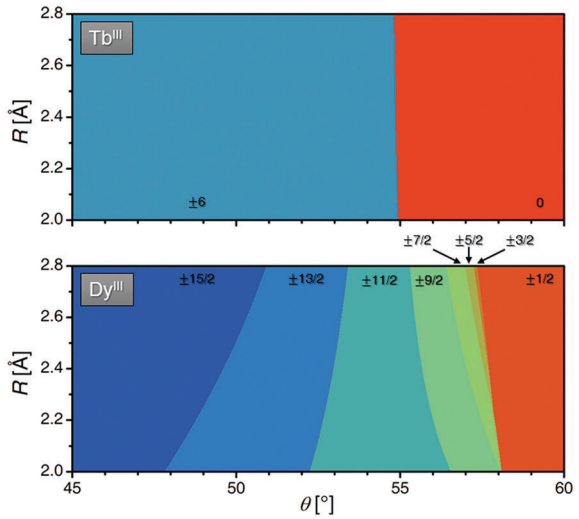


Scheme 16 Zenithal ($\theta$) dependence of the ground $m_J$ states with different Ln–X distances for $Tb^{III}$ and $Dy^{III}$. This scheme is calculated based on eqn (2.5).

$Pc^{2-}$ ligands may fall into this vicinity and result in such an energy level crossing, as their actual position is not centred at the N atoms.

By systematically changing the substituting groups on $Pc^{2-}$ ligands, the local geometry and charge density can be altered for $Pc^{2-}$ ligands and extend the original $[Tb(Pc)_2]^-$ into a huge library.[110] Ideally, a $D_{4d}$ symmetry requires a twist angle ($\Phi$) of 45° between the two layers of ligands. However, in reality, the deviation from the perfect $D_{4d}$ symmetry introduces transverse CF terms and results in fast QTM at zero field. The nuclear spin of the central lanthanide ion also plays an important role for QTM by mixing and splitting the energy levels through hyperfine interactions, and multiple steps are observed on the magnetic hysteresis loops for the diluted $[Ln(Pc)_2]^-$ (Ln = Tb, Dy, Ho).[104,105] Furthermore, as the redox activity of Pc-derived ligands, the negatively-charged prototype can undergo a one-electron oxidation to a neutral radical product of $[Tb(Pc)_2]$,[111] or undergo a two-electron oxidation to a positively-charged product of $[Tb(Pc)_2]^+$.[112] As a result, energy barriers and coercive fields can be affected as well as QTM,[113] and [Ln(Pc)(Pc′)] is highlighted by an energy barrier of 939 K, although the magnetic hysteresis loop is closed at zero field.[114] Nevertheless, one should be very careful to compare the natural product with others: it is in fact a 2p–4f system including an $S = 1/2$ radical, which produces unneglectable splitting of the energy levels by magnetic interactions and further affects the relaxation behaviour.

A family of lanthanide polyoxometalates (POMs) with the formula of $Na_9[Ln(W_5O_{18})_2]$ is also a sandwich structure encapsulating a lanthanide ion in square antiprismatic geometry.[115] Among them, the $Er^{III}$ derivative shows a twist angle $\Phi$ of 44.2°, which is very close to the ideal $D_{4d}$ symmetry. Nevertheless, low-symmetry effects due to deviation from the idealized $D_{4d}$ local symmetry are still evidenced in the inelastic neutron scattering (INS) spectra.[116] The crystal-field parameters extracted from magnetic fitting indicate a ground state of $|m_J| = 13/2$, with low-lying excited states of $|m_J| = 1/2$ and $|m_J| = 15/2$. Although the energy barrier of 55.2 K is not very high, it shows nice out-of-phase peaks up to 6.2 K (10 000 Hz). Compared with $[Er(Pc)_2]^-$ that has a ground state of $|m_J| = 1/2$, here the coordination atoms are closer to the equatorial plane with a zenithal angle $\theta$ of almost 60°. Therefore, the larger $|m_J|$ states of $Er^{III}$ can be stabilized (Scheme 2), but those of $Tb^{III}$ and $Dy^{III}$ will be high above and our estimation suggests that the ground state is $|m_J| = 0$ for $Tb^{III}$ and $|m_J| = 11/2$ or 9/2 for $Dy^{III}$. These results correspond well with those of the crystal-field fitting,[117] which may explain why they both do not show slow relaxation of magnetization. On the other hand, the ground state for the $Ho^{III}$ derivative is found to be $|m_J| = 4$, which shows significant tunnelling gaps in the presence of hyperfine splitting and enables multiple EPR transitions.[103,104]

### 4.2 $C_{5h}/D_{5h}$

$C_{5h}/D_{5h}$ is one of the five classes of point-charge symmetries in which all transverse CF terms vanish. We should emphasise again that the symmetry principal axis should coincide with the magnetic anisotropy axis, in order to minimize the transverse CFs. For example, in the pentagonal-bipyramid-like $[Dy(L)Cl_2(THF)_2]$ (L = $[2,6\text{-}(2,6\text{-}C_6H_3Et_2N{=}CH)_2\text{-}C_6H_3]^-$)[118] and the asymmetric dinuclear $[Dy_2(ovph)_2Cl_2(MeOH)_3]_3$ ($H_2ovph$ = ((2-hydroxy-3-methoxyphenyl)methylene)hydrazide),[119] the magnetic anisotropy axes lie approximately on the plane rather than the pseudo-$C_5$ axis, which could result from the stronger crystal fields on the equatorial plane. In addition, the mirror in the equatorial plane is also important. The polyoxometalate with monocapped pentagonal antiprism geometry ($C_5$ symmetry without $\sigma_h$), $[LnP_5W_{30}O_{110}]^{12-}$, gives rise to a large $|q| = 5$ CF parameter and mixed magnetic states. Therefore, fast spin–lattice relaxation and fast quantum tunnelling are observed.[120]

In 2013, a Ln-SIM with pentagonal–bipyramidal geometry, $[DyZn_2(TTTT^{Br})_2(MeOH)]^+$ ($\{DyZn_2\}_{D_{5h}}$, **1**), was first reported by Tong *et al.*[26] The compressed geometry (axial/equatorial: 2.21 Å/2.39 Å) favours the oblate-symmetric ion of $Dy^{III}$, in which the magnetic anisotropy axis goes through the 5-fold axis. The axial ligands largely stabilize the largest $|m_J| = 15/2$ doublet and amplify the energy gaps between the ground and the excited doublets. In addition, compared with 3-, 4- and 6-fold symmetries, the equatorial ligands arranged in a pseudo-5-fold symmetry are good for minimizing the transverse CFs and supressing QTM. Moreover, the long Dy–O/N distances on the plane are also very helpful, in spite of the unavoidable deviation from the symmetry of charge distribution in crystalline compounds.

Interestingly, **1** can reversibly transformed to the desolvated $[DyZn_2(TTTT^{Br})_2]^+$ ($\{DyZn_2\}_{O_h}$, **1′**), which possesses a compressed octahedral geometry (axial/equatorial: 2.19 Å/2.30 Å). Although the axial Dy–O distances of **1′** are both shorter than those of **1**, the much shorter equatorial Dy–O distances dramatically increase the transverse CFs, giving $g_{x,y} \approx 10^{-4}$ for **1**, while $g_{x,y} \approx 10^{-2}$ for **1′**. As a consequence, the effective energy barrier, relaxation times and hysteresis temperature are greatly reduced in **1′**. Furthermore, the relaxation mechanism turns from the Raman process to the Orbach one in the measured temperatures and fields. Experimental results and *ab initio* calculations both render the power of the $C_{5h}/D_{5h}$ symmetry strategy that can minimize the transverse CFs and increase the SMM performance (Fig. 2).

When the diamagnetic $Zn^{II}$ was replaced by the paramagnetic $Fe^{II}$,[121] the rarely-observed $Fe^{II}$–$Dy^{III}$ SMM, which is ferromagnetically coupled, shows a high energy barrier of 459 K. The Mössbauer spectrum reveals that the slowing down of $Fe^{II}$ relaxation times could be attributed to the frozen magnetic moment of $Dy^{III}$ at low temperatures. For the $Co^{II}$ analogue,[122] its magnetic dynamics vary sensitively to the outer coordination environments. $[DyCo_2(TTTT^{Br})_2(H_2O)]NO_3$ achieves the highest effective energy barrier (600 K) among the d–f heterometallic SMMs reported to date. However, the quantum tunnelling limits their performances, which could mainly be due to the magnetic dipolar interaction that originated from the neighbouring transition-metal ions.

A solvent-free SMM with thermal and air stability deserves to be realized with the aim of depositing the molecules on surfaces.[123] [Dy(bbpen)X] (X = Cl (**2**), Br (**2′**)) are highly stable

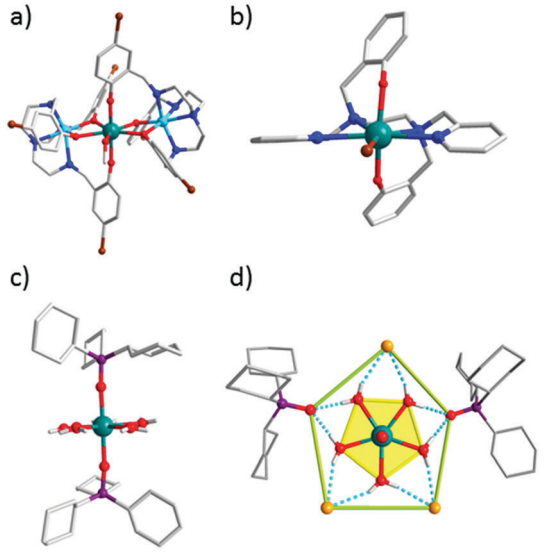


Fig. 2 Molecular structures of $[DyZn_2(TTTT^{Br})_2(MeOH)]^+$ (a), [Dy(bbpen)Br] (b) and $[Dy(OPCy_3)_2(H_2O)_5]^{3+}$ (c and d).

and neutral coordination complexes.[99] By the introduction of a stronger axial CF (2.16 Å) and a weaker transverse CF in the pentagonal-bipyramidal coordination environment, the effective energy barrier makes a breakthrough of over 1000 K *via* the 3rd excited doublet, accompanied by an open hysteresis at 14 K. Complex **2′** has a longer Dy–Br bond and smaller transverse CFs than **2**, shedding light on the importance of weakening the equatorial coordination ligands in experiment.

For $[Dy(O^tBu)_2(py)_5]^+$ (**3**),[124] the axial Dy–O lengths (2.11 Å) are the shortest found in all seven-coordinate Dy complexes, which are bonded by the negatively charged *tert*-butoxide, and the equatorial Dy–N bonds are long (2.56 Å) with quite regular $C_{5h}/D_{5h}$ symmetry (CShM value: 0.801). All the aforementioned factors lead to a giant effective energy barrier of 1815 K *via* the highly bunched set of excited doublets, along with the high ZFC peak temperature (14 K) under 0.2 T. In fact, this energy barrier is similar to that of the $[Dy(Cp^{ttt})_2]^+$ (1837 or 1760 K).[18,19]

In pursuit of $C_{5h}/D_{5h}$ symmetry, a family of $[Dy(OPR_3)_2(H_2O)_5]^{3+}$ SMMs[100,125,126] is among the good candidates, one of which ($[Dy(OPCy_3)_2(H_2O)_5]Br_3{\cdot}2(Cy_3PO){\cdot}2H_2O{\cdot}2EtOH$[100]) possesses the most perfect $D_{5h}$ coordination sphere ever reported (CShM value: 0.142, O–Dy–O angle: 179.04°). In this family, the axial Dy–O bonds (2.19–2.22 Å) are not as short as those of **2**, **2′** and **3**, and the equatorial Dy–O bonds are not long enough (2.33–2.38 Å). Therefore the effective energy barriers are only in the 472–735 K range. On the other hand, the hysteresis temperatures and ZFC peak temperatures are among the highest reported and comparable to those with more oblate coordination spheres, thanks to their very regular $C_{5h}/D_{5h}$ symmetries that largely suppress the QTM. This is supported by the downgraded performance of the Cl analogue, whose CShM value is a little bit larger (0.239) owing to the asymmetric hydrogen bonds in the secondary coordination sphere. In addition, the fluorescence spectra for one of them provide abundant information about the energy levels which are consistent with the magnetic measurements.[126]

Due to the lack of assurance from the Kramers degeneracy, non-Kramers SIMs were rarely reported compared with the Kramers SIMs. Thanks to the near-perfect $C_{5h}/D_{5h}$ symmetry of $[Ln(OPR_3)_2(H_2O)_5]^{3+}$, the $Ho^{III}$ analogue unveils the slow relaxation of magnetization under zero field, with the highest effective barrier (341 K) among $Ho^{III}$ SIMs.[106] Moreover, hyperfine structures/multiple steps of the single-crystal hysteresis were clearly observed, in addition to the field-dependent relaxation time extracted from the AC magnetic susceptibility. Interestingly, QTM is greatly minimized in the absence of a magnetic field and the QTM is moved to the in-field area, which is attributed to the interplay between the near-perfect $C_{5h}/D_{5h}$ symmetry and the hyperfine interaction arising from $^{165}Ho$ ($I$ = 7/2). This result indicates that the zero-field QTM can be suppressed by the coupling between the $^{165}Ho$ half-integer nuclear spin and its integer electron spin, hampering the reversal of magnetization.

### 4.3 $C_{3v}$

For equatorial three-coordinate Ln-SIMs, if the perfect planar $C_{3h}$ symmetry is adopted, all transverse CFs will be eliminated except for the $|q|$ = 6 (Table 2) terms. However, $[Er\{N(SiMe_3)_2\}_3]$ only has a symmetry of $C_{3v}$ because the $Er^{III}$ ion is out of the equatorial plane (Fig. 3a and b),[127,128] and the $|q|$ = 3 terms still remain unquenched as discussed in Section 2.3, which was also analysed by experimental spectroscopy.[129] It is clear that the $|m_J|$ order is in accord with the quadrupole approximation described in Section 2.2, from the largest to the smallest for $Er^{III}$; while the order reverses for the $Dy^{III}$ analogue.[130] Tang *et al.* reported the magnetic dynamics of these low-coordinate lanthanide complexes,[127] and slow relaxation of magnetization in the absence of a magnetic field was clearly observed. In contrast, the much faster relaxation/QTM for the $Dy^{III}$ analogue originates from the $|m_J|$ = 1/2 ground doublet.

### 4.4 $C_{6h}/D_{6h}$

In theory, the presence of 6-fold symmetry only persists the transverse CF terms of $|q|$ = 6. In particular, for $Ce^{III}$ and $Sm^{III}$

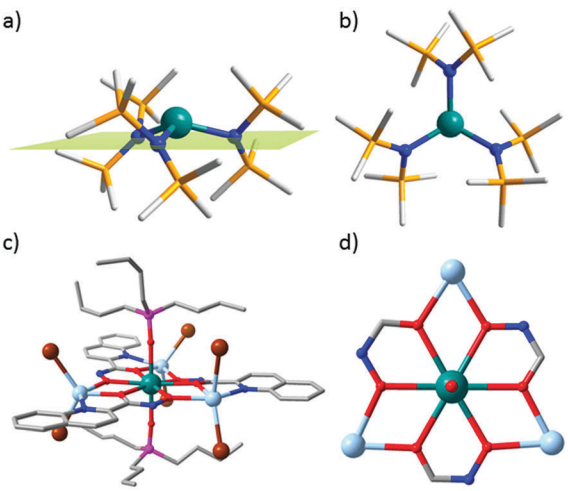


Fig. 3 Molecular/core structures of $[Er\{N(SiMe_3)_2\}_3]$ (a and b) and $[LnCd_3(Hquinha)_3(^nBu_3PO)_2I_3]$ (c and d). The N3 plane of $[Er\{N(SiMe_3)_2\}_3]$ is highlighted as green.

ions with a small $J$ = 5/2, all terms should vanish. Hence a hexagonal bipyramidal geometry is expected to be beneficial for $Ce^{III}$/$Sm^{III}$-SMMs. There have been several macrocyclic complexes with an equatorial six-coordinate environment reported, like {$Zn_3Er$},[131] {$Zn_3Dy$},[132] {$Cu_3Tb$},[133] {$Cd_3Ln$} (Ln = Ce and Nd)[88] and so on,[134,135] but only five of them exhibit SMM behaviours.[88,131–133]

Among them, [$LnCd_3$(Hquinha)$_3$($^n$$Bu_3PO$)$_2I_6$] ({$Cd_3Ln$}, Fig. 3c and d) based on 15-metallacrown-6 is the only one with eight-coordinate hexagonal-bipyramidal geometry, which is close to $C_{6h}/D_{6h}$ symmetry.[88] The axial and equatorial Ln–O bonds fall in 2.29–2.36 Å and 2.48–2.54 Å. Although the coordination sphere is compressed, the numbers of equatorial hydroximate oxygens and the axial phosphinyl oxygens are 6 and 2, respectively. The competition between them gives a ground doublet with an intermediate $|m_J|$ = 3/2 for $Ce^{III}$ (Scheme 2). The ground doublet of $Ce^{III}$ should have been pure under perfect 6-fold rotation symmetry. However, the deviation from the $C_6$ symmetry introduces small but unneglectable transverse magnetic anisotropy ($g_x$ = 0.02, $g_y$ = 0.10). For $Nd^{III}$, the $|q|$ = 6 term that cannot vanish even in perfect $C_6$ symmetry mixes magnetic states with $\Delta m_J$ = 6. Therefore the ground doublet is an admixture of $m_J = \pm 9/2$ and $m_J = \mp 3/2$, giving even larger transverse magnetic anisotropy ($g_x$ = 0.07, $g_y$ = 0.27) compared with that of the $Ce^{III}$ analogue. As a consequence, QTM prevents the presence of slow magnetic relaxation at zero field, and the Raman process is dominant under an applied field. Moreover, the magnetic relaxation for the $Ce^{III}$ analogue is slower than that of $Nd^{III}$ in the range of measured temperatures, possibly owing to its smaller transverse magnetic anisotropy as discussed above.

### 4.5 $C_\infty$

In 2011, Gao *et al.* reported the first organometallic Ln-SIM, [(Cp*)Er(COT)] (Fig. 4a), which can be described as pseudo-$C_\infty$ symmetric.[15,136,137] The two effective energy barriers for this slightly tilting sandwich-type SMM are assigned to the two conformers of the rotatable COT ring. Because of the special aromatic rings of Cp* and COT, the experimental results can be reproduced by the lone pair effective charge (LPEC) model instead of the PCE model,[63] suggesting that the ligand effective charges are not localized on the carbon centres. This is important for stabilizing the largest $|m_J|$ = 15/2 ground doublet of the prolate-symmetric $Er^{III}$ ion.

By replacing Cp* into boratabenzene, the [($C_5H_5BMe$)Er(COT)] features the highest energy barrier (432 K) among $Er^{III}$ SIMs.[138] By the utilization of the poorer electron donor, an improved energy barrier can be explained by weakening the negative contribution from the axial positions for prolate-symmetric $Er^{III}$. For the family of β-diketonate- and cyclomultiene-supported $Dy^{III}$ SIMs, the magnetic anisotropy axes are perpendicular to the pseudo-axial direction.[139] By fine tuning the substituent Cp, the transverse magnetic anisotropy can become fairly small by accident even without the promise of symmetry, as discussed in Section 2.3. In such a case, the transverse magnetic anisotropy would be very sensitive to any subtle changes in coordination environments.

Constructed by dianionic $COT^{2-}$ or its derivative together with $Ln^{III}$, a series of Ln-COT SMMs with pseudo-$C_8$ or pseudo-$C_\infty$ symmetry including the sandwich-type $[Ln(COT)_2]^-$ (Fig. 4b)[140–144] and the triple-decker $[Ln_2(COT)_3]$[145,146] were reported by Murugesu *et al.* and Long *et al.* Similar to the $D_{4d}$ $[Ln(Pc)_2]$ SMMs, the energy levels for both $[Ln(COT)_2]^-$ are crossing and not strictly proportional to the $|m_J|$ order,[142] suggesting that the charge distribution of the ligands is close to the "magic angle" as shown in Schemes 2 and 16. For the $Dy^{III}$ ones, the $|m_J|$ = 15/2 doublet is destabilized and becomes the highest excited doublet, which is in contrast to the case of $Er^{III}$. In addition, the substituent groups could also break the symmetry of charge distribution. The significant derivation between the magnetic anisotropy axis and the pseudo-$C_8$ rotation axis destructs the systematic absences of transverse crystal-field terms for $C_8$ symmetry in Table 2.[142,145] As a result, the magnetic hysteresis loop is closed due to the fast QTM arising from the highly mixed ground doublet and large transverse magnetic anisotropy.

In comparison with $Dy^{III}$, the SMM performance improves much when using $Er^{III}$ ions.[140–142] The stabilization of the $|m_J|$ = 15/2 doublet accompanied by the collinearity of the magnetic anisotropy axis and the pseudo-$C_8$ axis enables the rule of the symmetry strategy. Accordingly, the $g_{x,y}$ is dramatically decreased from $10^{-1}$ for $Dy^{III}$ to $10^{-6}$ for $Er^{III}$, which is indicative of the strong suppression of QTM in $[Er(COT)_2]^-$.

The most amazing SMM reported to date is the $[Dy(Cp^{ttt})_2]^+$ dysprosocenium (Fig. 4c and d) reported by Mills *et al.* and Layfield *et al.*, exceeding all previous SMMs for the high hysteresis temperature up to 60 K.[18,19] Although the $Cp_C$–Dy–$Cp_C$ bend angle ($Cp_C$ is defined as the $Cp^{ttt}$ centre) is 153°, it is worth mentioning that the two $Cp^{ttt}$ are closely eclipsed rather than staggered from the top view, roughly along the magnetic anisotropy axis. The geometry is just like a pentagonal prism with pseudo $C_{5h}/D_{5h}$ symmetry (Fig. 4d). Large axial magnetic

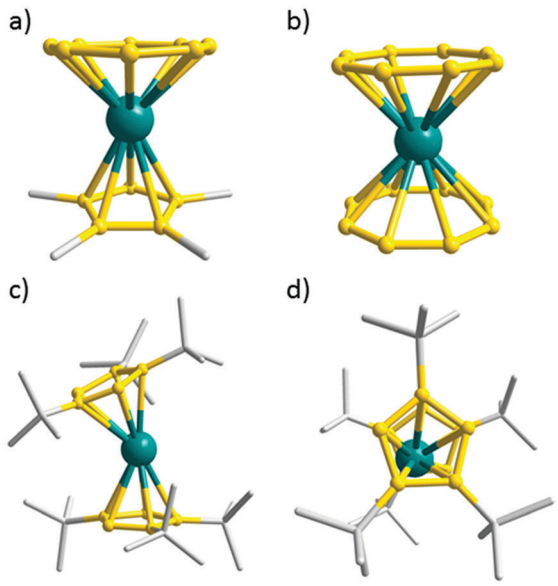


Fig. 4 Molecular structures of [(Cp*)Er(COT)] (a), $[Er(COT)_2]^-$ (b) and $[Dy(Cp^{ttt})_2]^+$ (c and d). The aromatic rings are highlighted as yellow.

anisotropy and neglectable transverse magnetic anisotropy may come from the near axial symmetry of the delocalized aromatic electrons. In addition, the small-ring $Cp^{ttt}$ could lead to concentrated effective charges with small zenithal angles ($\theta$), thus efficiently enhancing the axial magnetic anisotropy and minimizing the transverse magnetic anisotropy. As a result, the reversal of magnetization is greatly blocked for the $[Dy(Cp^{ttt})_2]^+$ complex. This is further evidenced by that of the starting material, $[Dy(Cp^{ttt})_2Cl]$, which is significantly downgraded by the equatorial negatively-charged $Cl^-$. The experimental result coincides with the hypothetical $[Dy(Cp^*)_2]^+$ model and the suggested strategy of weakening the equatorial ancillary ligands.[147] *Ab initio* spin dynamics suggest the C–H vibration on the $Cp^{ttt}$ ligand facilitates the initial $|m_J| = 15/2 \rightarrow |m_J| = 13/2$ relaxation step, but the bulky substituent groups here restrict the vibrational motion, thus possibly slowing down the relaxation rates.[18] Recently, the electronic structures and magnetic properties of other heavy lanthanide analogues were reported. Compared with the pseudo-equatorial CFs provided by large-ring COT, the small-ring $Cp^{ttt}$ results in more pseudo-axial CFs. Therefore, it is no surprise that the ground state of $Ho^{III}$ is as large as $|m_J| = 7$ (mixed with $|m_J| = 8$), but the ground states of $Er^{III}$, $Tm^{III}$ and $Yb^{III}$ are those with small $|m_J|$.[73]

Endohedral metallofullerenes (EMFs), when encapsulating anisotropic lanthanide ions, facilitate a unique family of Ln-SMMs. Starting from a $DySc_2N@C_{80}$ SIM[148] to the magnetically coupled $Dy_2TiC@C_{80}$,[149] and finally to the $Dy_2ScN@C_{80}$ showing an energy barrier of 1735 K,[150] they all possess a relatively pure ground doublet of $|m_J| = 15/2$. A closer look at the local coordination environment of $Dy^{III}$ in the crystal structure (Fig. 5b) reveals that the negative charges provided by the nitrogen atom and the $C_{80}$ cage are located near the axial position, while the equatorial plane is virtually empty. Such a pseudo-$C_\infty$ symmetry not only stabilizes the largest $|m_J|$ doublet, but also leads to a relatively pure $m_J$ composition for several higher states, enabling $Dy_2ScN@C_{80}$ to relax through the 5th excited Kramers doublet for an individual $Dy^{III}$.[150] Rather interesting progress in this family recently is trapping an unpaired electron into a single-electron Dy–Dy bond in $Dy_2@C_{80}$.[151] Giant exchange interactions are observed along with huge anisotropy as before, which promotes an experimental $\tau$ = 100 s at 18 K despite the moderate energy barrier of 613 K.

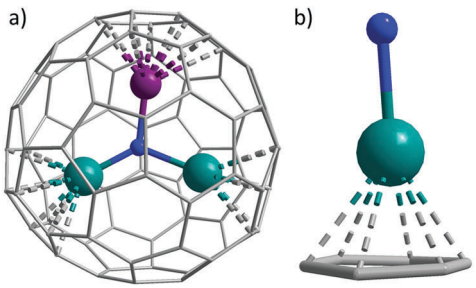


Fig. 5 Molecular structure of $Dy_2ScN@C_{80}$ (a) and the local coordination environment of $Dy^{III}$ (b).

### 4.6 Others

Finally, let's take a look at some other cases that should not be simply categorized into the symmetries discussed above. β-Diketonate $Ln^{III}$ complexes, with the general formula of $[Ln(acac)_{2-3}L_{2-5}]$ including some auxiliary ligands (L), represent a large family in mononuclear lanthanide SMMs. The prototype $[Dy(acac)_3(H_2O)_2]$ started such a trend by $|m_J| = 13/2$ states, a moderate energy barrier and a butterfly-shaped hysteresis loop when diluted in $Y^{III}$.[152] However, the following systematically replacement of the auxiliary ligands in $[Ln(paaH)_2L_4]$ (Ln = Tb, Dy, Ho, Er, paaH = *N*-(2-pyridyl)-ketoacetamide) indicates that it favours only $Dy^{III}$ by stabilizing its $|m_J| = 15/2$ states.[153] A theoretical calculation on the β-diketonate system sheds light on such a trend that the magnetic anisotropy axis of $Dy^{III}$ points near one of the negative oxygen atoms of β-diketonate, perpendicular to the weakest plane formed by natural auxiliary ligands.[154] Therefore, simply interpreting the β-diketonate system by a geometric $D_{4d}$ symmetry regardless of the charge distribution can be misleading. In other words, the success of the β-diketonate system largely relies on the axial magnetic anisotropy of the electrostatic potentials (Section 2.2), while the further symmetry requirements fail to meet. As a result, the QTM around zero field is usually fast despite that some of them have a pseudo-$\sigma_h$ or $\sigma_v$ symmetry, which still exists when diluted and/or even the nuclear-spin-free isotopes are used (Fig. 6).[107,108]

Similar conclusions can also be applied to many decent Ln-SMMs with high anisotropy but insufficient local symmetry. A series of low-symmetry $\{DyZn_2\}$ complexes, in which the $Dy^{III}$ ion is nine-coordinate including four negative phenol oxygen atoms located near the axial position, exhibit high energy barriers up to 430 K, but all of them show butterfly-shaped hysteresis loops.[155]

The pyramidal $[Dy_5O(O^iPr)_{13}]$ with six-coordinate $Dy^{III}$ ions in pseudo-$C_{4v}$ symmetry represents one of the most anisotropic coordination environments highlighted by a Dy-terminal alkoxide bond as short as 1.95 Å.[156] However, there is a mismatch between

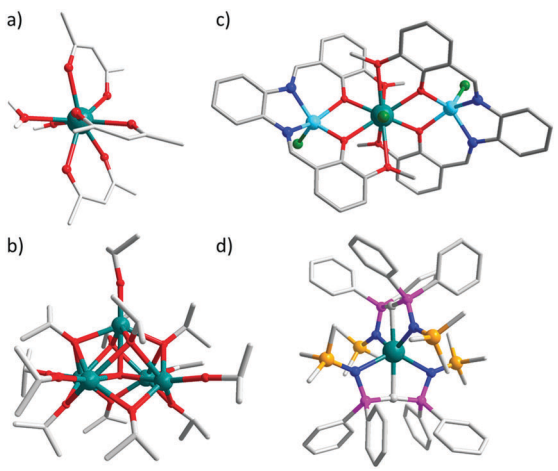


Fig. 6 Molecular structures of $[Dy(acac)_3(H_2O)_2]$ (a), $[Zn_2(sal_2opd)_2DyCl_3]$ (b), $[Dy_5O(O^iPr)_{13}]$ (c) and $[Dy(BIPM^{TMS})_2]^-$ (d).

the absence of hysteresis loops and the high energy barrier of 528 K, and the $Ho^{III}$ derivative ($U_{eff}$ ~400 K) only exhibits partial relaxation.[157] For the similar $[Dy_4K_2O(O^tBu)_{12}]$, the energy barrier increases to 692 K (842 K for a diluted sample). The intermetallic magnetic interactions play mixed roles here as the exchange bias of QTM is eliminated upon dilution and create a step at zero field.[158]

In $[Dy(BIPM^{TMS})_2]^-$, the $Dy^{III}$ ion is also six-coordinate, but close to an $S_4/D_{2d}$ symmetry that can eliminate all transverse terms except for $|q| = 4$. In addition to this, two highly negative methanediides in opposite directions stabilize virtually pure $|m_J| = 15/2$ states. Two energy barriers are observed as 721 K and 813 K, and the in-field behaviours are nice including a noticeable divergence of ZFC–FC curves below 16 K.[159] Nevertheless, the QTM at zero field remains clear even for a diluted sample, and we foresee that these systems could still be better if stricter symmetry strategies are employed.

The $N_2^{3-}$ radical-bridged dilanthanide complexes represented by $[Ln_2(N_2)\{N(SiMe_3)_2\}_4(THF)_2]^-$ (Ln = Dy, Tb) have been acting as benchmark SMMs owing to their high magnetic blocking temperatures (14 K for $\tau$ = 100 s) and large coercive fields.[94,95] Compared with the poor properties of the reduced non-radical $N_2^{2-}$-bridged analogue, it is evidenced that the key factor in this system is the extremely strong direct exchange coupling between the $N_2^{3-}$ radical and dilanthanide ions, rather than a strict local symmetry. Nevertheless, DFT and *ab initio* calculations suggest that such strong exchange interactions can efficiently mix the ground and the first excited exchange states, which may largely facilitate the relaxation *via* the first excited states rather than higher ones.[160] Also, strong axial anisotropy enforced by suitable CFs is still necessary to provide large enough energy splitting on the Ln sites and reduce the QTM between ground states. In the most recent case using Cp-derivative ligands, further enhancement of the axial symmetry is achieved by the removal of coordinating THF molecules.[95] As a result, the relaxation time for the Dy-analogue boosts by more than three orders of magnitude at 2 K, and the 100 s blocking temperature for the Tb-analogue increases to 20 K with a significantly enlarged $\tau_0$ value. Anyway, it is still important but challenging to synergistically make use of magnetic exchange and magnetic anisotropy.

Last but not least, for some cases with lower local symmetry, significant variation in the magnetic anisotropy could be induced by small differences in coordination geometry, such as the distortion of ligands,[161–163] the rotation of the hydrogen atoms on coordinated water molecules[45] or even the exchange of uncoordinated lattice solvents.[164] Although it may be difficult to design these systems into high performance SMMs, their easily tuned magnetic response could be beneficial for molecular sensors and switches.

## 5. Conclusions and outlook

In this review, the intuitive effective charge model is introduced to help understand the magnetic states of $Ln^{III}$, qualitatively explaining the oblate-/prolate-symmetric preferences and the energy level crossings. When allocating the ligand charges around the "magic angle" of 54.7°, easy-axis/plane anisotropy could gradually switch to its opposite type of magnetic anisotropy, giving rise to an intermediate $|m_J|$ ground doublet. In further consideration of the transverse magnetic anisotropy which is vital for spin–lattice relaxation and quantum tunnelling of magnetization, the symmetry strategy of using specific groups of symmetries, including $C_n$ ($n \geq 7$), $S_8/D_{4d}$, $C_{5h}/D_{5h}$ and $S_{12}/D_{6d}$, is summarized, in order to minimize the transverse CFs and take advantage for designing high-performance SMMs. Although these groups of symmetries are physically forbidden in conventional crystals, Ln-SMMs in most of the near-perfect symmetries have been achieved experimentally and most of them exhibit impressive magnetic dynamics, as demonstrated in this review. Challenging but interesting, the synthesis of Ln-SMMs in $S_{12}/D_{6d}$ symmetry that can potentially eliminate transverse CFs remains unexplored (Table 2).

To fulfil the symmetry strategy, several important points are necessary, which are mentioned again: (1) in order to minimize the transverse CFs, the most contributed direction, namely the magnetic anisotropy axis for the ground $|m_J|$, should coincide with the principal symmetry axis; (2) the charge centres are not necessary localized on the coordinates of the coordination atoms, especially for the ligands with delocalized electrons; and (3) the charge density distribution is more essential for the symmetry strategy rather than the molecular geometry.

Although there are many challenges in the characterization of these excellent Ln-SMMs satisfactorily employing the symmetry strategies, their dynamic magnetism can be understood by the numerical solution of the Bloch equation. It is demonstrated that different techniques of AC susceptibility, decay of magnetization, magnetic hysteresis and ZFC/FC magnetization, all present certain aspects of the slow relaxation of magnetization. Anyway, magnetic blocking occurs whenever the magnetic relaxation is slower than the alteration of environment variables such as temperature and fields, and it is highly dependent on the experimental parameters instead of being a certain critical point. We believe that the discussion on the practical magnetic characterization and the clarification on certain issues here would help relieve some confusion and hereafter facilitate the further exploration of high-performance SMMs.

Nevertheless, there are still many open questions and challenges to be addressed. For example:

(1) Are there any treasures covered among the unexplored or uncommon $Ln^{III}$, instead of the widely reported $Dy^{III}$, $Tb^{III}$ and $Er^{III}$?

(2) How to improve the SMM performances with single-ion anisotropy and magnetic interactions synergistically?

(3) What is the role of nuclear spin? Can we make use of it to improve the magnetic dynamics?

(4) What is the role of covalent bonds in Ln-SMMs and how important is it to affect the magnetic anisotropy?

(5) Can we obtain the chemically stable and neutral Ln-SMMs with comparable SMM performances to others, in order to better serve the applications in spintronics?

(6) How do molecular vibrations affect the dynamic CFs and spin–phonon coupling?

And these questions await the endeavours from all of our talented fellows to answer in the upcoming decades.

## Conflicts of interest

There are no conflicts to declare.

## Acknowledgements

This work was supported by the NSFC (Grant no. 21620102002, 21773316, 21371183, 91422302 and 21701198), the Fundamental Research Funds for the Central Universities (Grant 17lgjc13 and 17lgpy81) and the China Postdoctoral Science Foundation (National Postdoctoral Program for Innovative Talents, Grant BX201700295).

## Notes and references

1 R. Sessoli, D. Gatteschi, A. Caneschi and M. A. Novak, *Nature*, 1993, **365**, 141–143.
2 R. Sessoli, H. L. Tsai, A. R. Schake, S. Wang, J. B. Vincent, K. Folting, D. Gatteschi, G. Christou and D. N. Hendrickson, *J. Am. Chem. Soc.*, 1993, **115**, 1804–1816.
3 W. Wernsdorfer and R. Sessoli, *Science*, 1999, **284**, 133–135.
4 M. N. Leuenberger and D. Loss, *Nature*, 2001, **410**, 789–793.
5 D. Gatteschi, R. Sessoli and R. Villain, *Molecular Nanomagnets*, Oxford University Press, New York, 2006.
6 L. Bogani and W. Wernsdorfer, *Nat. Mater.*, 2008, **7**, 179–186.
7 M. Mannini, F. Pineider, P. Sainctavit, C. Danieli, E. Otero, C. Sciancalepore, A. M. Talarico, M.-A. Arrio, A. Cornia, D. Gatteschi and R. Sessoli, *Nat. Mater.*, 2009, **8**, 194–197.
8 S. Thiele, F. Balestro, R. Ballou, S. Klyatskaya, M. Ruben and W. Wernsdorfer, *Science*, 2014, **344**, 1135–1138.
9 R. Sessoli and A. K. Powell, *Coord. Chem. Rev.*, 2009, **253**, 2328–2341.
10 P. Zhang, Y.-N. Guo and J. Tang, *Coord. Chem. Rev.*, 2013, **257**, 1728–1763.
11 D. N. Woodruff, R. E. P. Winpenny and R. A. Layfield, *Chem. Rev.*, 2013, **113**, 5110–5148.
12 H. L. C. Feltham and S. Brooker, *Coord. Chem. Rev.*, 2014, **276**, 1–33.
13 R. Layfield, *Organometallics*, 2014, **33**, 1084–1099.
14 K. Liu, X. Zhang, X. Meng, W. Shi, P. Cheng and A. K. Powell, *Chem. Soc. Rev.*, 2016, **45**, 2423–2439.
15 Y.-S. Meng, S.-D. Jiang, B.-W. Wang and S. Gao, *Acc. Chem. Res.*, 2016, **49**, 2381–2389.
16 F. Pointillart, O. Cador, B. Le Guennic and L. Ouahab, *Coord. Chem. Rev.*, 2017, **346**, 150–175.
17 S. G. McAdams, A.-M. Ariciu, A. K. Kostopoulos, J. P. S. Walsh and F. Tuna, *Coord. Chem. Rev.*, 2017, **346**, 216–239.
18 C. A. P. Goodwin, F. Ortu, D. Reta, N. F. Chilton and D. P. Mills, *Nature*, 2017, **548**, 439–442.
19 F.-S. Guo, B. M. Day, Y.-C. Chen, M.-L. Tong, A. Mansikkamäki and R. A. Layfield, *Angew. Chem., Int. Ed.*, 2017, **56**, 11445–11449.
20 L. Sorace, C. Benelli and D. Gatteschi, *Chem. Soc. Rev.*, 2011, **40**, 3092–3104.
21 N. F. Chilton, D. Collison, E. J. L. McInnes, R. E. P. Winpenny and A. Soncini, *Nat. Commun.*, 2013, **4**, 2551.
22 M. T. Hutchings, *Solid State Phys.*, 1964, **16**, 227–273.
23 A. Abragam and B. Bleaney, *Electron paramagnetic resonance of transition ions*, Clarendon Press, Oxford, 1970.
24 C. A. Morrison and R. P. Leavitt, in *Handbook on the Physics and Chemistry of Rare Earths*, ed. K. A. Gschneidner, Jr. and L. Eyring, 1982, ch. 46, vol. 5.
25 C. Görller-Walrand and K. Binnemans, in *Handbook on the Physics and Chemistry of Rare Earths*, ed. K. A. Gschneidner, Jr. and L. Eyring, 1996, ch. 155, vol. 23.
26 J.-L. Liu, Y.-C. Chen, Y.-Z. Zheng, W.-Q. Lin, L. Ungur, W. Wernsdorfer, L. F. Chibotaru and M.-L. Tong, *Chem. Sci.*, 2013, **4**, 3310.
27 H. A. Kramers, *Proc. K. Ned. Akad. Wet.*, 1930, **33**, 959–972.
28 D. J. Griffiths, *Introduction to Quantum Mechanics*, Pearson Prentice Hall, 2nd edn, 2005.
29 O. Kahn, *Molecular Magnetism*, Wiley-VCH, New York, 1993.
30 H. A. Bethe, *Ann. Phys.*, 1929, **3**, 133–206.
31 D. J. Newman, *Adv. Phys.*, 2006, 197–256.
32 O. L. Malta, S. J. L. Ribeiro, M. Faucher and P. Porcher, *J. Phys. Chem. Solids*, 1991, **52**, 587–593.
33 J. J. Baldoví, Y. Duan, R. Morales, A. Gaita-Ariño, E. Ruiz and E. Coronado, *Chem. – Eur. J.*, 2016, **22**, 13532–13539.
34 L. Ungur and L. F. Chibotaru, *Chem. – Eur. J.*, 2017, **23**, 3708–3718.
35 J. D. Jackson, *Classical Electrodynamics*, John Wiley & Sons, Inc., 3rd edn, 1999.
36 J. Sievers, *Z. Phys. B: Condens. Matter*, 1982, **45**, 289–296.
37 S. Edvardsson and M. Klintenberg, *J. Alloys Compd.*, 1998, **275-277**, 230–233.
38 K. W. H. Stevens, *Proc. Phys. Soc., London, Sect. A*, 1952, **65**, 209.
39 U. Walter, *Z. Phys. B: Condens. Matter*, 1986, **62**, 299–309.
40 D. Schimitt, *J. Phys.*, 1986, **47**, 677–681.
41 R. Skomski, *Simple Models of Magnetism*, Oxford University Press, New York, 2008.
42 J. D. Rinehart and J. R. Long, *Chem. Sci.*, 2011, **2**, 2078–2085.
43 L. F. Chibotaru and L. Ungur, *J. Chem. Phys.*, 2012, **137**, 64112.
44 L. F. Chibotaru, *Struct. Bonding*, 2015, **164**, 185–230.
45 G. Cucinotta, M. Perfetti, J. Luzon, M. Etienne, P.-E. Car, A. Caneschi, G. Calvez, K. Bernot and R. Sessoli, *Angew. Chem., Int. Ed.*, 2012, **51**, 1606–1610.
46 M. E. Boulon, G. Cucinotta, J. Luzon, C. Degl'Innocenti, M. Perfetti, K. Bernot, G. Calvez, A. Caneschi and R. Sessoli, *Angew. Chem., Int. Ed.*, 2013, **52**, 350–354.

 

47 K. Qian, J. J. Baldví, S.-D. Jiang, A. Gaita-Ariño, Y.-Q. Zhang, J. Overgaard, B.-W. Wang, E. Coronado and S. Gao, *Chem. Sci.*, 2015, **6**, 4587–4593.
48 S.-D. Jiang and S.-X. Qin, *Inorg. Chem. Front.*, 2015, **2**, 613–619.
49 P. Panissod and M. Drillon, in *Magnetism: Molecules to Materials IV*, ed. J. S. Miller and M. Drillon, Wiley-VCH Verlag GmbH & Co. KGaA, Weinheim, 2002, ch. 7.
50 J.-D. Leng, J.-L. Liu, W.-Q. Lin, S. Gómez-Coca, D. Aravena, E. Ruiz and M.-L. Tong, *Chem. Commun.*, 2013, **49**, 9341–9343.
51 N. Ishikawa, M. Sugita, T. Okubo, N. Tanaka, T. Iino and Y. Kaizu, *Inorg. Chem.*, 2003, **42**, 2440–2446.
52 M. Merhring and J. S. Waugh, *Phys. Rev. B: Solid State*, 1972, **5**, 3459.
53 S. J. Erickson, R. W. Prost and M. E. Timins, *Radiology*, 1993, **188**, 23–25.
54 J. Jensen and A. R. Mackintosh, *Rare Earth Magnetism*, Clarendon Press, Oxford, 1991.
55 R. J. Elliott, *Magnetic Properties of Rare Earth Metals*, Plenum Publishing Corporation, New York, 1972.
56 J. J. Baldoví, J. M. Clemente-Juan, E. Coronado, A. Gaita-Ariño and A. Palii, *J. Comput. Chem.*, 2014, **35**, 1930–1934.
57 J. J. Baldoví, S. Cardona-Serra, J. M. Clemente-Juan, E. Coronado, A. Gaita-Ariño and A. Palii, *J. Comput. Chem.*, 2013, **34**, 1961–1967.
58 J. J. Baldoví, J. J. Borrás-Almenar, J. M. Clemente-Juan, E. Coronado and A. Gaita-Ariño, *Dalton Trans.*, 2012, **41**, 13705.
59 I. D. Ryabov, *J. Magn. Reson.*, 1999, **140**, 141–145.
60 C. Rudowicz and C. Y. Chung, *J. Phys.: Condens. Matter*, 2004, **16**, 5825–5847.
61 S. Stoll and A. Schweiger, *J. Magn. Reson.*, 2006, **178**, 42–55.
62 N. F. Chilton, R. P. Anderson, L. D. Turner, A. Soncini and K. S. Murray, *J. Comput. Chem.*, 2013, **34**, 1164–1175.
63 J. J. Baldoví, J. M. Clemente-Juan, E. Coronado and A. Gaita-Ariño, *Inorg. Chem.*, 2014, **53**, 11323–11327.
64 J. J. Baldoví, Y. Duan, C. Bustos, S. Cardona-Serra, P. Gouzerh, R. Villanneau, G. Gontard, J. M. Clemente-Juan, A. Gaita-Ariño, C. Giménez-Saiz, A. Proust and E. Coronado, *Dalton Trans.*, 2016, **45**, 16653–16660.
65 L. Ungur and L. F. Chibotaru, *Inorg. Chem.*, 2016, **55**, 10043–10056.
66 D. Gatteschi and R. Sessoli, *Angew. Chem., Int. Ed.*, 2003, **42**, 268.
67 L. Landau, *Phys. Z. Sowjetunion*, 1932, **4**, 46.
68 C. Zener, *Proc. R. Soc. London, Ser. A*, 1932, **137**, 696.
69 C. Wittig, *J. Phys. Chem. B*, 2005, **109**, 8428–8430.
70 E. del Barco, A. D. Kent, S. Hill, J. M. North, N. S. Dalal, E. M. Rumberger, D. N. Hendrickson, N. Chakov and G. Christou, *J. Low Temp. Phys.*, 2005, **140**, 119–174.
71 H. Fröhlich, *Proc. R. Soc. London, Ser. A*, 1952, **215**, 291–298.
72 N. F. Chilton, *Inorg. Chem.*, 2015, **54**, 2097–2099.
73 C. A. P. Goodwin, D. Reta, F. Ortu, N. F. Chilton and D. P. Mills, *J. Am. Chem. Soc.*, 2017, **139**, 18714–18724.
74 A. Lunghi, F. Totti, R. Sessoli and S. Sanvito, *Nat. Commun.*, 2016, **8**, 14620.
75 M. Atzori, L. Tesi, S. Benci, A. Lunghi, R. Righini, A. Taschin, R. Torre, L. Sorace and R. Sessoli, *J. Am. Chem. Soc.*, 2017, **139**, 4338–4341.
76 S. T. Liddle and J. van Slageren, *Chem. Soc. Rev.*, 2015, **44**, 6655–6669.
77 K. W. H. Stevens, *Rep. Prog. Phys.*, 1967, **30**, 189.
78 R. D. Mattuck and M. W. P. Strandberg, *Phys. Rev.*, 1960, **119**, 1204–1217.
79 R. Orbach, *Proc. R. Soc. London, Ser. A*, 1961, **264**, 458–484.
80 K. N. Shrivastava, *Phys. Status Solidi B*, 1983, **117**, 437–458.
81 K. N. Shrivastava, *Phys. Status Solidi B*, 1972, **51**, 377–387.
82 F. Hartmann-Boutron, P. Politi and J. Villain, *Int. J. Mod. Phys. B*, 1996, **10**, 2577.
83 D. A. Garanin and E. M. Chudnovsky, *Phys. Rev. B: Condens. Matter Mater. Phys.*, 1997, **56**, 11102–11118.
84 M. N. Leuenberger and D. Loss, *Phys. Rev. B: Condens. Matter Mater. Phys.*, 2000, **61**, 1286–1302.
85 J. M. Zadrozny, M. Atanasov, A. M. Bryan, C.-Y. Lin, B. D. Rekken, P. P. Power, F. Neese and J. R. Long, *Chem. Sci.*, 2013, **4**, 125–138.
86 M. Atanasov, J. M. Zadrozny, J. R. Long and F. Neese, *Chem. Sci.*, 2013, **4**, 139–156.
87 Y.-N. Guo, G.-F. Xu, Y. Guo and J. Tang, *Dalton Trans.*, 2011, **40**, 9953–9963.
88 Q.-W. Li, R.-C. Wan, Y.-C. Chen, J.-L. Liu, L.-F. Wang, J.-H. Jia, N. F. Chilton and M.-L. Tong, *Chem. Commun.*, 2016, **52**, 13365–13368.
89 Z.-X. Jiang, J.-L. Liu, Y.-C. Chen, J. Liu, J.-H. Jia and M.-L. Tong, *Chem. Commun.*, 2016, **52**, 6261–6264.
90 E. Lucaccini, J. J. Baldoví, L. Chelazzi, A.-L. Barra, F. Grepioni, J.-P. Costes and L. Sorace, *Inorg. Chem.*, 2017, **56**, 4728–4738.
91 K. S. Pedersen, J. Dreiser, H. Weihe, R. Sibille, H. V. Johannesen, M. A. Sørensen, B. E. Nielsen, M. Sigrist, H. Mutka, S. Rols, J. Bendix and S. Piligkos, *Inorg. Chem.*, 2015, **54**, 7600–7606.
92 J.-L. Liu, K. Yuan, J.-D. Leng, L. Ungur, W. Wernsdorfer, F.-S. Guo, L. F. Chibotaru and M.-L. Tong, *Inorg. Chem.*, 2012, **51**, 8538–8544.
93 Q.-W. Li, J.-L. Liu, J.-H. Jia, Y.-C. Chen, J. Liu, L.-F. Wang and M.-L. Tong, *Chem. Commun.*, 2015, **51**, 10291–10294.
94 J. D. Rinehart, M. Fang, W. J. Evans and J. R. Long, *J. Am. Chem. Soc.*, 2011, **133**, 14236–14239.
95 S. Demir, M. I. Gonzalez, L. E. Darago, W. J. Evans and J. R. Long, *Nat. Commun.*, 2017, **8**, 2144.
96 K. C. Mondal, A. Sundt, Y. Lan, G. E. Kostakis, O. Waldmann, L. Ungur, L. F. Chibotaru, C. E. Anson and A. K. Powell, *Angew. Chem., Int. Ed.*, 2012, **51**, 7550–7554.
97 K. C. Mondal, G. E. Kostakis, Y. Lan, W. Wernsdorfer, C. E. Anson and A. K. Powell, *Inorg. Chem.*, 2011, **50**, 11604–11611.
98 N. Ishikawa, M. Sugita, T. Ishikawa, S.-y. Koshihara and Y. Kaizu, *J. Am. Chem. Soc.*, 2003, **125**, 8694–8695.

99 J. Liu, Y.-C. Chen, J.-L. Liu, V. Vieru, L. Ungur, J.-H. Jia, L. F. Chibotaru, Y. Lan, W. Wernsdorfer, S. Gao, X.-M. Chen and M.-L. Tong, *J. Am. Chem. Soc.*, 2016, **138**, 5441–5450.
100 Y.-C. Chen, J.-L. Liu, L. Ungur, J. Liu, Q.-W. Li, L.-F. Wang, Z.-P. Ni, L. F. Chibotaru, X.-M. Chen and M.-L. Tong, *J. Am. Chem. Soc.*, 2016, **138**, 2829–2837.
101 E. M. Pineda, N. F. Chilton, R. Marx, M. Dörfel, D. O. Sells, P. Neugebauer, S.-D. Jiang, D. Collison, J. van Slageren, E. J. L. McInnes and R. E. P. Winpenny, *Nat. Commun.*, 2014, **5**, 5243.
102 M. Shiddiq, D. Komijani, Y. Duan, A. Gaita-Ariño, E. Coronado and S. Hill, *Nature*, 2016, **531**, 348–351.
103 S. Ghosh, S. Datta, L. Friend, S. Cardona-Serra, A. Gaita-Arino, E. Coronado and S. Hill, *Dalton Trans.*, 2012, **41**, 13697–13704.
104 N. Ishikawa, M. Sugita and W. Wernsdorfer, *Angew. Chem., Int. Ed.*, 2005, **44**, 2931–2935.
105 N. Ishikawa, M. Sugita and W. Wernsdorfer, *J. Am. Chem. Soc.*, 2005, **127**, 3650–3651.
106 Y.-C. Chen, J.-L. Liu, W. Wernsdorfer, D. Liu, L. F. Chibotaru, X.-M. Chen and M.-L. Tong, *Angew. Chem., Int. Ed.*, 2017, **56**, 4996–5000.
107 F. Pointillart, K. Bernot, S. Golhen, B. Le Guennic, T. Guizouarn, L. Ouahab and O. Cador, *Angew. Chem., Int. Ed.*, 2015, **54**, 1504–1507.
108 Y. Kishi, F. Pointillart, B. Lefeuvre, F. Riobe, B. Le Guennic, S. Golhen, O. Cador, O. Maury, H. Fujiwara and L. Ouahab, *Chem. Commun.*, 2017, **53**, 3575–3578.
109 S. Alvarez, P. Alemany, D. Casanova, J. Cirera, M. Llunell and D. Avnir, *Coord. Chem. Rev.*, 2005, **249**, 1693–1708.
110 H. Wang, B.-W. Wang, Z. Bian, S. Gao and J. Jiang, *Coord. Chem. Rev.*, 2016, **306**, 195–216.
111 N. Ishikawa, M. Sugita, N. Tanaka, T. Ishikawa, S.-y. Koshihara and Y. Kaizu, *Inorg. Chem.*, 2004, **43**, 5498–5500.
112 S. Takamatsu, T. Ishikawa, S.-y. Koshihara and N. Ishikawa, *Inorg. Chem.*, 2007, **46**, 7250–7252.
113 M. Gonidec, E. S. Davies, J. McMaster, D. B. Amabilino and J. Veciana, *J. Am. Chem. Soc.*, 2010, **132**, 1756–1757.
114 C. R. Ganivet, B. Ballesteros, G. de la Torre, J. M. Clemente-Juan, E. Coronado and T. Torres, *Chem. – Eur. J.*, 2013, **19**, 1457–1465.
115 M. A. AlDamen, J. M. Clemente-Juan, E. Coronado, C. Martí-Gastaldo and A. Gaita-Ariño, *J. Am. Chem. Soc.*, 2008, **130**, 8874–8875.
116 M. Vonci, M. J. Giansiracusa, W. Van den Heuvel, R. W. Gable, B. Moubaraki, K. S. Murray, D. Yu, R. A. Mole, A. Soncini and C. Boskovic, *Inorg. Chem.*, 2017, **56**, 378–394.
117 M. A. AlDamen, S. Cardona-Serra, J. M. Clemente-Juan, E. Coronado, A. Gaita-Ariño, C. Martí-Gastaldo, F. Luis and O. Montero, *Inorg. Chem.*, 2009, **48**, 3467–3479.
118 Y.-N. Guo, L. Ungur, G. E. Granroth, A. K. Powell, C. Wu, S. E. Nagler, J. Tang, L. F. Chibataru and D. Cui, *Sci. Rep.*, 2014, **4**, 5471.
119 Y.-N. Guo, G.-F. Xu, W. Wernsdorfer, L. Ungur, Y. Guo, J. Tang, H.-J. Zhang, L. F. Chibotaru and A. K. Powell, *J. Am. Chem. Soc.*, 2011, **133**, 11948–11951.
120 S. Cardona-Serra, J. M. Clemente-Juan, E. Coronado, A. Gaita-Ariño, A. Camón, M. Evangelisti, F. Luis, M. J. Martínez-Pérez and J. Sesé, *J. Am. Chem. Soc.*, 2012, **134**, 14982–14990.
121 J.-L. Liu, J.-Y. Wu, Y.-C. Chen, V. Mereacre, A. K. Powell, L. Ungur, L. F. Chibotaru, X.-M. Chen and M.-L. Tong, *Angew. Chem., Int. Ed.*, 2014, **53**, 12966–12970.
122 J.-L. Liu, J.-Y. Wu, G.-Z. Huang, Y.-C. Chen, J.-H. Jia, L. Ungur, L. F. Chibotaru, X.-M. Chen and M.-L. Tong, *Sci. Rep.*, 2015, **5**, 16621.
123 R. Sessoli, *Nature*, 2017, **548**, 400–401.
124 Y.-S. Ding, N. F. Chilton, R. E. P. Winpenny and Y.-Z. Zheng, *Angew. Chem., Int. Ed.*, 2017, **55**, 16071–16074.
125 S. K. Gupta, T. Rajeshkumar, G. Rajaraman and R. Murugavel, *Chem. Sci.*, 2016, **7**, 5181–5191.
126 Y.-C. Chen, J.-L. Liu, Y. Lan, Z.-Q. Zhong, A. Mansikkamäki, L. Ungur, Q.-W. Li, J.-H. Jia, L. F. Chibotaru, J.-B. Han, W. Wernsdorfer, X.-M. Chen and M.-L. Tong, *Chem. – Eur. J.*, 2017, **23**, 5708–5715.
127 P. Zhang, L. Zhang, C. Wang, S. Xue, S.-Y. Lin and J. Tang, *J. Am. Chem. Soc.*, 2014, **136**, 4484–4487.
128 W. A. Herrmann, R. Anwander, F. C. Munck, W. Scherer, V. Dufaud, N. W. Huber and G. R. J. Artus, *Z. Naturforsch., B: J. Chem. Sci.*, 1994, **49**, 1789–1797.
129 S. Jank, H. D. Amberger and N. M. Edelstein, *Spectrochim. Acta, Part A*, 1998, **54**, 1645–1650.
130 S. Jank, H. Reddmann and H. D. Amberger, *Inorg. Chim. Acta*, 2008, **361**, 2154–2158.
131 A. Yamashita, A. Watanabe, S. Akine, T. Nabeshima, M. Nakano, T. Yamamura and T. Kajiwara, *Angew. Chem., Int. Ed.*, 2011, **50**, 4016–4019.
132 H. L. C. Feltham, Y. Lan, F. Klöwer, L. Ungur, L. F. Chibotaru, A. K. Powell and S. Brooker, *Chem. – Eur. J.*, 2011, **17**, 4362–4365.
133 H. L. C. Feltham, R. Clérac, A. K. Powell and S. Brooker, *Inorg. Chem.*, 2011, **50**, 4232–4234.
134 H. L. C. Feltham, R. Clérac, L. Ungur, V. Vieru, L. F. Chibotaru, A. K. Powell and S. Brooker, *Inorg. Chem.*, 2012, **51**, 10603–10612.
135 H. L. C. Feltham, S. Dhers, M. Rouzières, R. Clérac, A. K. Powell and S. Brooker, *Inorg. Chem. Front.*, 2015, **2**, 982–990.
136 S.-D. Jiang, B.-W. Wang, H.-L. Sun, Z.-M. Wang and S. Gao, *J. Am. Chem. Soc.*, 2011, **133**, 4730–4733.
137 S.-D. Jiang, S.-S. Liu, L.-N. Zhou, B.-W. Wang, Z.-M. Wang and S. Gao, *Inorg. Chem.*, 2012, **51**, 3079–3087.
138 Y.-S. Meng, C.-H. Wang, Y.-Q. Zhang, X.-B. Leng, B.-W. Wang, Y.-F. Chen and S. Gao, *Inorg. Chem. Front.*, 2016, **3**, 828–835.
139 S.-S. Liu, L. Xu, S.-D. Jiang, Y.-Q. Zhang, Y.-S. Meng, Z. Wang, B.-W. Wang, W.-X. Zhang, Z. Xi and S. Gao, *Inorg. Chem.*, 2015, **54**, 5162–5168.
140 M. Jeletic, P.-H. Lin, J. J. Le Roy, I. Korobkov, S. I. Gorelsky and M. Murugesu, *J. Am. Chem. Soc.*, 2011, **133**, 19286–19289.
141 K. R. Meihaus and J. R. Long, *J. Am. Chem. Soc.*, 2013, **135**, 17952–17957.

 

142 L. Ungur, J. J. Le Roy, I. Korobkov, M. Murugesu and L. F. Chibotaru, *Angew. Chem., Int. Ed.*, 2014, **53**, 4413–4417.
143 J. J. Le Roy, I. Korobkova and M. Murugesu, *Chem. Commun.*, 2014, **50**, 1602–1604.
144 J. J. Le Roy, I. Korobkov, J. E. Kim, E. J. Schelter and M. Murugesu, *Dalton Trans.*, 2014, **43**, 2737–2740.
145 J. J. Le Roy, M. Jeletic, S. I. Gorelsky, I. Korobkov, L. Ungur, L. F. Chibotaru and M. Murugesu, *J. Am. Chem. Soc.*, 2013, **135**, 3502–3510.
146 J. J. Le Roy, L. Ungur, I. Korobkov, L. F. Chibotaru and M. Murugesu, *J. Am. Chem. Soc.*, 2014, **136**, 8003–8010.
147 Y.-S. Meng, Y.-Q. Zhang, Z.-M. Wang, B.-W. Wang and S. Gao, *Chem. – Eur. J.*, 2016, **22**, 12724–12731.
148 R. Westerström, J. Dreiser, C. Piamonteze, M. Muntwiler, S. Weyeneth, H. Brune, S. Rusponi, F. Nolting, A. Popov, S. Yang, L. Dunsch and T. Greber, *J. Am. Chem. Soc.*, 2012, **134**, 9840–9843.
149 K. Junghans, C. Schlesier, A. Kostanyan, N. A. Samoylova, Q. Deng, M. Rosenkranz, S. Schiemenz, R. Westerström, T. Greber, B. Büchner and A. A. Popov, *Angew. Chem., Int. Ed.*, 2015, **54**, 13411–13415.
150 D. S. Krylov, F. Liu, S. M. Avdoshenko, L. Spree, B. Weise, A. Waske, A. U. B. Wolter, B. Büchnera and A. A. Popov, *Chem. Commun.*, 2017, **53**, 7901–7904.
151 F. Liu, D. S. Krylov, L. Spree, S. M. Avdoshenko, N. A. Samoylova, M. Rosenkranz, A. Kostanyan, T. Greber, A. U. B. Wolter, B. Büchner and A. A. Popov, *Nat. Commun.*, 2017, **8**, 16098.
152 S.-D. Jiang, B.-W. Wang, G. Su, Z.-M. Wang and S. Gao, *Angew. Chem., Int. Ed.*, 2010, **49**, 7448–7451.
153 N. F. Chilton, S. K. Langley, B. Moubaraki, A. Soncini, S. R. Battena and K. S. Murray, *Chem. Sci.*, 2013, **4**, 1719–1730.
154 D. Aravena and E. Ruiz, *Inorg. Chem.*, 2013, **52**, 13770–13778.
155 W.-B. Sun, P.-F. Yan, S.-D. Jiang, B.-W. Wang, Y.-Q. Zhang, H.-F. Li, P. Chen, Z.-M. Wang and S. Gao, *Chem. Sci.*, 2016, **7**, 684–691.
156 R. J. Blagg, C. A. Muryn, E. J. L. McInnes, F. Tuna and R. E. P. Winpenny, *Angew. Chem., Int. Ed.*, 2011, **50**, 6530–6533.
157 R. J. Blagg, F. Tuna, E. J. L. McInnes and R. E. P. Winpenny, *Chem. Commun.*, 2011, **47**, 10587.
158 R. J. Blagg, L. Ungur, F. Tuna, J. Speak, P. Comar, D. Collison, W. Wernsdorfer, E. J. L. McInnes, L. F. Chibotaru and R. E. P. Winpenny, *Nat. Chem.*, 2013, **5**, 673–678.
159 M. Gregson, N. F. Chilton, A.-M. Ariciu, F. Tuna, I. F. Crowe, W. Lewis, A. J. Blake, D. Collison, E. J. L. McInnes, R. E. P. Winpenny and S. T. Liddle, *Chem. Sci.*, 2016, **7**, 155–165.
160 V. Vieru, N. Iwahara, L. Ungur and L. F. Chibotaru, *Sci. Rep.*, 2016, **6**, 24046.
161 L.-F. Wang, J.-Z. Qiu, J.-L. Liu, Y.-C. Chen, J.-H. Jia, J. Jover, E. Ruiz and M.-L. Tong, *Chem. Commun.*, 2015, **51**, 15358–15361.
162 L.-F. Wang, J.-Z. Qiu, J.-Y. Hong, Y.-C. Chen, Q.-W. Li, J.-H. Jia, J. Jover, E. Ruiz, J.-L. Liu and M.-L. Tong, *Inorg. Chem.*, 2017, **56**, 8829–8836.
163 L.-F. Wang, J.-Z. Qiu, Y.-C. Chen, J.-L. Liu, Q.-W. Li, J.-H. Jia and M.-L. Tong, *Inorg. Chem. Front.*, 2017, **4**, 1311–1318.
164 X. Zhang, V. Vieru, X. Feng, J.-L. Liu, Z. Zhang, B. Na, W. Shi, B.-W. Wang, A. K. Powell, L. F. Chibotaru, S. Gao, P. Cheng and J. R. Long, *Angew. Chem., Int. Ed.*, 2015, **54**, 9861–9865.